

The Radius-Luminosity Relationship Depends on Optical Spectra in Active Galactic Nuclei

PU DU¹ AND JIAN-MIN WANG^{1,2,3}

¹Key Laboratory for Particle Astrophysics, Institute of High Energy Physics, Chinese Academy of Sciences, 19B Yuquan Road, Beijing 100049, China

²National Astronomical Observatories of China, Chinese Academy of Sciences, 20A Datun Road, Beijing 100020, China

³School of Astronomy and Space Science, University of Chinese Academy of Sciences, 19A Yuquan Road, Beijing 100049, China

ABSTRACT

The radius-luminosity ($R_{\text{H}\beta}$ - L_{5100}) relationship of active galactic nuclei (AGNs) established by the reverberation mapping (RM) observations has been widely used as a single-epoch black hole mass estimator in the research of large AGN samples. However, the recent RM campaigns discovered that the AGNs with high accretion rates show shorter time lags by factors of a few comparing with the predictions from the $R_{\text{H}\beta}$ - L_{5100} relationship. The explanation of the shortened time lags has not been finalized yet. We collect 8 different single-epoch spectral properties to investigate how the shortening of the time lags correlate with those properties and to understand what is the origin of the shortened lags. We find that the flux ratio between Fe II and H β emission lines shows the most prominent correlation, thus confirm that accretion rate is the main driver for the shortened lags. In addition, we establish a new scaling relation including the relative strength of Fe II emission. This new scaling relation can provide less biased estimates of the black hole mass and accretion rate from the single-epoch spectra of AGNs.

Keywords: galaxies: active; galaxies: nuclei - quasars: supermassive black holes

1. INTRODUCTION

In the past 40 years, reverberation mapping (RM; e.g., Bahcall et al. 1972; Blandford & McKee 1982; Peterson et al. 1993) has become a powerful tool to investigate the geometry and kinematics of the broad-line regions (BLRs) in active galactic nuclei (AGNs) and to measure the masses of supermassive black holes (BHs). Through long-term spectroscopic monitoring of an AGN, the size scale (R_{BLR}) of its BLR can be directly obtained by measuring the delayed response (τ_{BLR}) of the emission line with respect to the variation of the continuum, where $R_{\text{BLR}} = c\tau_{\text{BLR}}$ and c is the speed of light. Fortunately, the RM observations of ~ 100 objects (e.g., Peterson et al. 1993, 1998, 2002, 2004; Kaspi et al. 2000, 2007; Bentz et al. 2008, 2009a; Denney et al. 2009; Barth et al. 2011, 2013, 2015; Rafter et al. 2011, 2013; Du et al. 2014, 2015, 2016a, 2018a,b; Wang et al. 2014a; Shen et al. 2016b; Fausnaugh et al. 2017; Grier et al. 2012, 2017b; De Rosa et al. 2018; Woo et al. 2019) lead to a correlation between the time lag of H β emission line (or the radius $R_{\text{H}\beta}$ of the H β -emitting region) and the monochromatic luminosity (λL_{λ}) at 5100 Å (hereafter L_{5100}) with the form of

$$R_{\text{H}\beta} = \alpha \ell_{44}^{\beta}, \quad (1)$$

where $\ell_{44} = L_{5100}/10^{44}$ erg s⁻¹ (e.g., Kaspi et al. 2000; Bentz et al. 2009b, 2013). This correlation makes it possible to estimate BLR radius from a single-epoch spectrum. It is called the $R_{\text{H}\beta}$ - L_{5100} relationship, and has been widely adopted as a single-epoch BH mass estimator in the research of large AGN samples (e.g., McLure & Dunlop 2004; Vestergaard & Peterson 2006; Kollmeier et al. 2006; Greene & Ho

2007; Shen et al. 2011). However, there is growing evidence for increasing scatters of the $R_{\text{H}\beta}$ - L_{5100} relationship from ongoing RM campaigns.

Reverberation of broad emission lines to the continuum confirms photoionization as the major radiation mechanism in the BLR. As a canonic model of BLR, photoionization defined by the ionization parameter $\Xi \propto L_{\text{ion}}/R_{\text{BLR}}^2 n_e T$ directly indicates $R_{\text{BLR}} \propto L_{\text{ion}}^{1/2}$, where L_{ion} is the ionizing luminosity, n_e and T are electron density and temperature of the ionized gas, respectively. If we take L_{5100} as a proxy of L_{ion} , we have $R_{\text{BLR}} \propto L_{5100}^{1/2}$, agreeing with the observations (see also Bentz et al. 2013). We would like to emphasize here the necessary conditions for this canonic relation: (1) ionizing source should be isotropic or at least quasi-isotropic so that the BLR clouds receive the same luminosity with observers; (2) $L_{\text{ion}} \propto L_{5100}$ should always work; (3) ionizing luminosity comes from a point source, which is much smaller than the distances of the BLR clouds to the central BH. Condition (1) is broken in the AGNs powered by slim accretion disks (Wang et al. 2014c), where the puffed-up inner region may lead to non-isotropic ionizing radiation (Wang et al. 2014c). Condition (2) relies on spectral energy distributions (only holds for pro-grade accretion AGNs powered by the Shakura-Sunyaev disks), and does not work in ones with retro-grade accretion (Wang et al. 2014b; Czerny et al. 2019). Low spin (also low accretion rate and large BH mass) may lead to the deficit of the UV photons and non-linear relation between L_{ion} and L_{5100} (Wang et al. 2014b; Czerny et al. 2019). And the L_{5100} variation shows a little lag with respect to the L_{ion} variation in the RM of accretion

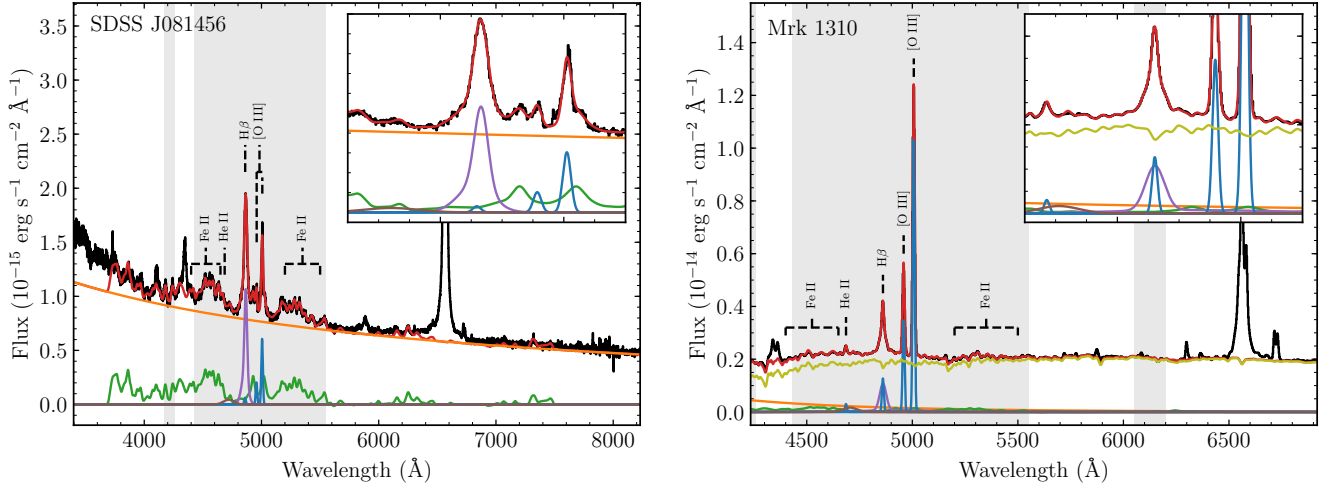


Figure 1. Two fitting examples. In each panel, the black line is the spectrum in the rest frame after Galactic extinction correction. The red line is the best fit. The orange line is the power law of the continuum. The purple line is the broad $H\beta$ component. The blue lines are the narrow emission lines ($[O\ III]\lambda\lambda 4959, 5007, H\beta$, and $He\ II$). The green, brown, and yellow lines are the $Fe\ II$ template, broad $He\ II$, and the template of host galaxy, respectively. The zoom-in panels show the detailed fitting around $H\beta$. Some strong emission lines are labeled.

disks (Edelson et al. 2015; McHardy et al. 2018; Cackett et al. 2018, e.g.). About Condition (3), the size of accretion disk, although small, has been successfully measured and is not infinitesimal (Edelson et al. 2015; McHardy et al. 2018; Cackett et al. 2018). Therefore, the $R_{H\beta}-L_{5100}$ relationship is expected to depend on accretion situation or some other properties.

Recently, Super-Eddington Accreting Massive Black Hole (SEAMBH) campaign discovered that many objects with strong $Fe\ II$ and narrow $H\beta$ emission lines, which are thought to be the AGNs with high accretion rates, lie below the $R_{H\beta}-L_{5100}$ relationship (Du et al. 2015, 2016a, 2018a). They found that the time lags of the AGNs with high accretion rates become shortened by factors of $3 \sim 8$ relative to the normal-accretion-rate AGNs with the same luminosities, and the shortening itself shows correlation with the accretion rate (Du et al. 2015, 2016a, 2018a). Wang et al. (2014c) proposed that the anisotropic radiation of the slim accretion disk may probably result in the shortened time lags. The Sloan Digital Sky Survey Reverberation Mapping (SDSS-RM) Project also reported many AGNs have time lags shorter than expected from the $R_{H\beta}-L_{5100}$ relationship (Grier et al. 2017b), but cautioned that selection effects may arise at least in some cases (see Grier et al. 2019).

Although the detailed physical explanation causing the shortened time lags is not yet finalized (Wang et al. 2014c; Grier et al. 2017b, 2019), more and more objects deviating from the traditional $R_{H\beta}-L_{5100}$ relationship are being discovered (Grier et al. 2017b; Du et al. 2018a). It is urgent to investigate the origin of the shortened lags in more detail. In this paper, we investigate how the deviation of an AGN from the $R_{H\beta}-L_{5100}$ relationship correlates with the properties in the single-epoch spectrum, and try to establish a new scaling relationship including the influence of single-epoch spectral properties. We describe the sample, data, and mea-

surements in Section 2. A new scaling relation is established and presented in Section 3. Some discussions are provided in Section 4, and a brief summary is given in Section 5. We adopt the standard Λ CDM cosmology and the parameters of $H_0 = 67\text{ km s}^{-1}\text{ Mpc}^{-1}$, $\Omega_\Lambda = 0.68$, and $\Omega_m = 0.32$ (Planck Collaboration et al. 2014, 2018) in this paper.

2. DATA AND MEASUREMENT

2.1. Sample

The analysis in the present paper is mainly based on the samples: (1) the RM measurements compiled in Bentz et al. (2013) from the previous literatures, (2) the AGNs with high accretion rates of the SEAMBH campaign published in Du et al. (2014, 2015, 2016a, 2018a); Wang et al. (2014a); Hu et al. (2015), (3) some other AGNs published after 2013: Mrk 1511 from Barth et al. (2013), NGC 5273 from Bentz et al. (2014), KA 1858+4850 from (Pei et al. 2014), MCG +06-30-015 from (Bentz et al. 2016b; Hu et al. 2016), UGC 06728 from (Bentz et al. 2016a), and MCG +08-11-011, NGC 2617, 3C 382 and Mrk 374 from Fausnaugh et al. (2017)¹. The collection in Bentz et al. (2013) includes 41 AGNs monitored successively since the late 1980's, most of which have relatively weaker $Fe\ II$ emission and broader $H\beta$ lines compared to the SEAMBH objects (Du et al. 2018a). The SEAMBH campaign, as a dedicated RM project for AGNs with high accretion rates, published the time lags of 25 objects (totally 30 measurements, some objects have more than one measurement). Including the objects published after 2013, we have totally 75 objects with 117 measurements. The time lags,

¹ We also include the new RM observations of the previous mapped objects after 2013 in the following analysis: NGC 4593 (Barth et al. 2013), NGC 7469 (Peterson et al. 2014), NGC 5548 (Lu et al. 2016; Pei et al. 2017), NGC 4051 (Fausnaugh et al. 2017), PG 1226+023 (3C 273, Zhang et al. 2019), and PG 2130+099 (Hu et al. 2019)

5100Å, H β , and [O III] luminosities, equivalent width (EW) of H β and [O III], and H β FWHM of the corresponding campaigns are listed in Table 1. Some objects have been mapped more than once, in order to understand the population properties better, we have to equalize the weights of the individual objects in the following analysis. We average the multiple measurements by taking into account their measurement uncertainties (see more details in Du et al. 2015). The average measurements, etc. lags, FWHM, luminosities, are also listed in Table 1.

2.2. Data of Single-epoch Spectral Properties

To investigate how the single-epoch spectral properties control the deviation of AGNs from the $R_{\text{H}\beta}$ - L_{5100} relationship, we compile 8 different parameters from the spectra around the H β region in the optical band: (1) the flux ratio between Fe II and H β , which is denoted as

$$\mathcal{R}_{\text{Fe}} = F_{\text{Fe}}/F_{\text{H}\beta}, \quad (2)$$

where F_{Fe} is the flux of Fe II from 4434Å to 4684Å and $F_{\text{H}\beta}$ is the flux of broad H β , (2) FWHM of H β emission line ($\text{FWHM}_{\text{H}\beta}$), (3) equivalent width (EW) of [O III] λ 5007 emission line ($\text{EW}_{[\text{OIII}]}$), (4) the ratio between FWHM and σ_{line} (second moment of the line profile) of the H β line ($\mathcal{D}_{\text{H}\beta} = \text{FWHM}_{\text{H}\beta}/\sigma_{\text{H}\beta}$), (5) the ratio between the FWHM of Fe II and the FWHM of H β ($\text{FWHM}_{\text{Fe II}}/\text{FWHM}_{\text{H}\beta}$), (6) the asymmetry of H β line defined by $A = [\lambda_c(3/4) - \lambda_c(1/4)]/\text{FWHM}_{\text{H}\beta}$, where $\lambda_c(3/4)$ and $\lambda_c(1/4)$ are the central wavelengths at the 3/4 and 1/4 of the H β peak height (De Robertis 1985; Boroson & Green 1992; Brotherton 1996; Du et al. 2018b), (7) the EW of He II (EW_{HeII}), and (8) the EW of H β ($\text{EW}_{\text{H}\beta}$). These parameters are referred to as “single-epoch spectral properties”, because they can be measured simply from the single-epoch spectra rather than from the time-domain observations like RM². In order to establish some new scaling relationships which can be applied to the large AGN samples obtained in the spectroscopic surveys of SDSS or Dark Energy Spectroscopic Instrument (DESI) in the near future, we need to find the correlations between the single-epoch properties and the deviation of AGNs from the $R_{\text{H}\beta}$ - L_{5100} relationship. The FWHM and EW of the H β line, and the EW of the [O III] line of each RM campaign are collected and listed in Table 1. We use them (and the average values for the objects with multiple RM measurements) directly in the following analysis. We search the other parameters in the literatures and list the values in Table 2. For the parameters that we can not find in the literatures, we fit the spectra of the objects found in the public archive and measure those parameters by ourselves (see also Table 2).

2.3. Fitting the spectra

² Of course, if we have the RM data, we can definitely measure them from an individual spectrum in the RM campaign or the mean spectrum (can be treated as the average of the values from the individual spectra). But if we don't have the RM data, we can still measure them from the single-epoch spectra found in some other literatures or databases.

We use the following components in the spectral fitting: (1) a power law to model the AGN continuum, (2) two Gaussians to model the broad H β emission line, (3) a template constructed from the Fe II spectrum of the narrow-line Seyfert 1 (NLS1) galaxy I Zw 1 by Boroson & Green (1992) for the Fe II emission, (4) one or two Gaussians for each of the narrow emission lines, e.g., [O III] λ 4959,5007, H β , He II (if necessary), (5) one or two Gaussians to model the broad He II and (6) a simple stellar population model³ from Bruzual & Charlot (2003) as a template for the contribution of the host galaxy if necessary. The fitting is mainly performed in the windows of 4170–4260Å and 4430–5550Å in the rest frame. If the host contribution is significant, we supplement the window of 6050–6200Å to give a better constraint to the fitting of stellar template. All of the narrow-line components in each object are fixed to have the same velocity width and shift, except for those showing very different width/shift. [O III] λ 4959 is fixed to have one-third of the [O III] λ 5007 flux (Osterbrock & Ferland 2006). NLS1s always show very weak narrow emission lines (in particular, the narrow H β). In the fitting for the spectra of NLS1s, we also fix the flux of narrow H β to be one-tenth of the [O III] λ 5007 flux (Kewley et al. 2006; Stern & Laor 2013). Two examples (SDSS J081456 and Mrk 1310) of the multi-component spectral fitting are shown in Figure 1. The contribution of host galaxy in the spectrum of SDSS J081456 is weak, while Mrk 1310 is host-dominated. The fitting of these two objects are fairly good. We measure the spectral properties (see Section 2.2) from the fitting results and list them in Table 2.

3. ANALYSIS

3.1. Pairwise Correlations between Different Properties

Before discussing the correlations between the single-epoch spectral properties and the deviation from the $R_{\text{H}\beta}$ - L_{5100} relationship, we first present the pairwise correlations between different properties in Figure 2. Although there are many similar discussions using different samples in the historical literatures (e.g., Boroson & Green 1992), it is still valuable to do this demonstration for the RM objects. Spearman's rank correlation coefficients (ρ) and the corresponding two-sided p -value for a null hypothesis test (two sets of data are uncorrelated) are marked in the panels of Figure 2. The ρ and p values of the significant correlations (with $p < 0.001$) are marked with red color.

Among all of the correlations, $\text{FWHM}_{\text{H}\beta}$ versus $\mathcal{D}_{\text{H}\beta}$ is the most significant one, which has Spearman's correlation coefficient $\rho = 0.70$. It means that if the width of H β line is smaller, its profile tends to be more Lorentzian-like. This correlation has been demonstrated by, e.g., Kollatschny & Zetzl (2011, 2013). The sample in the present paper is larger than that used in Kollatschny & Zetzl (2011, 2013), but the result is almost the same. The secondarily-significant correlations are \mathcal{R}_{Fe} versus $\text{FWHM}_{\text{FeII}}/\text{FWHM}_{\text{H}\beta}$ ($\rho = 0.69$),

³ We select the simple stellar population model which can get the smallest χ^2 in the fitting.

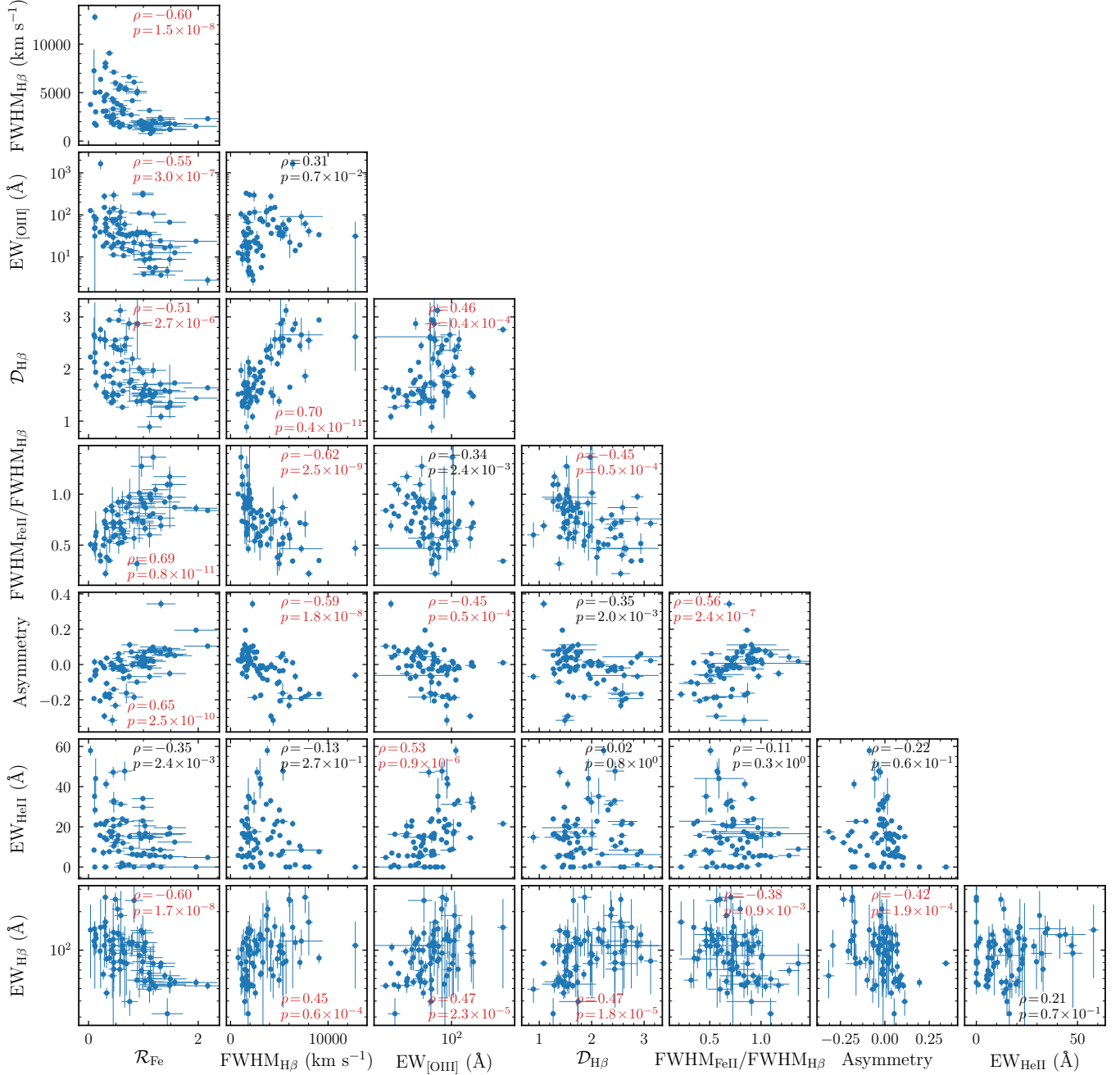


Figure 2. Pairwise correlations of the single-epoch spectral properties for the sample in the present paper. The Spearman’s rank correlation coefficients (ρ) and the corresponding null probabilities (see Section 3.1) are marked in the corner of each panel (with red color if $p < 0.001$).

\mathcal{R}_{Fe} versus $\text{H}\beta$ Asymmetry ($\rho = 0.65$), \mathcal{R}_{Fe} versus $\text{EW}_{\text{H}\beta}$ ($\rho = -0.60$), \mathcal{R}_{Fe} versus $\text{FWHM}_{\text{H}\beta}$ ($\rho = -0.60$), and $\text{FWHM}_{\text{H}\beta}$ versus $\text{FWHM}_{\text{Fe II}}/\text{FWHM}_{\text{H}\beta}$ ($\rho = -0.62$). The previous three correlations mean that, if the relative strength of Fe II is higher, the widths of Fe II and $\text{H}\beta$ are more similar, $\text{H}\beta$ line tends to have stronger blue wing, and the EW of $\text{H}\beta$ line is weaker. Similar to the correlation between \mathcal{R}_{Fe} and $\text{FWHM}_{\text{Fe II}}/\text{FWHM}_{\text{H}\beta}$, $\text{FWHM}_{\text{H}\beta}$ versus $\text{FWHM}_{\text{Fe II}}/\text{FWHM}_{\text{H}\beta}$ means that the objects with narrower $\text{H}\beta$ lines also have more similar Fe II and $\text{H}\beta$ widths.

In addition, the correlations of \mathcal{R}_{Fe} versus $\text{EW}_{[\text{OIII}]}$, \mathcal{R}_{Fe} versus $\mathcal{D}_{\text{H}\beta}$, $\text{FWHM}_{\text{H}\beta}$ versus $\text{H}\beta$ Asymmetry, $\text{EW}_{[\text{OIII}]}$ versus EW_{HeII} , and $\text{FWHM}_{\text{Fe II}}/\text{FWHM}_{\text{H}\beta}$ versus $\text{H}\beta$ Asymmetry are also significant. \mathcal{R}_{Fe} versus ($\text{FWHM}_{\text{H}\beta}$ and $\text{EW}_{[\text{OIII}]}$) are the prominent correlations in the famous AGN eigenvector 1 sequence (e.g., Boroson & Green 1992; Sulentic et al. 2000; Marziani et al. 2001, 2003, 2018; Shen & Ho 2014; Sun, & Shen 2015). The detailed physical process of this sequence is still under some debate (e.g., Panda et al. 2019). The correlation between \mathcal{R}_{Fe} versus $\text{H}\beta$ Asym-

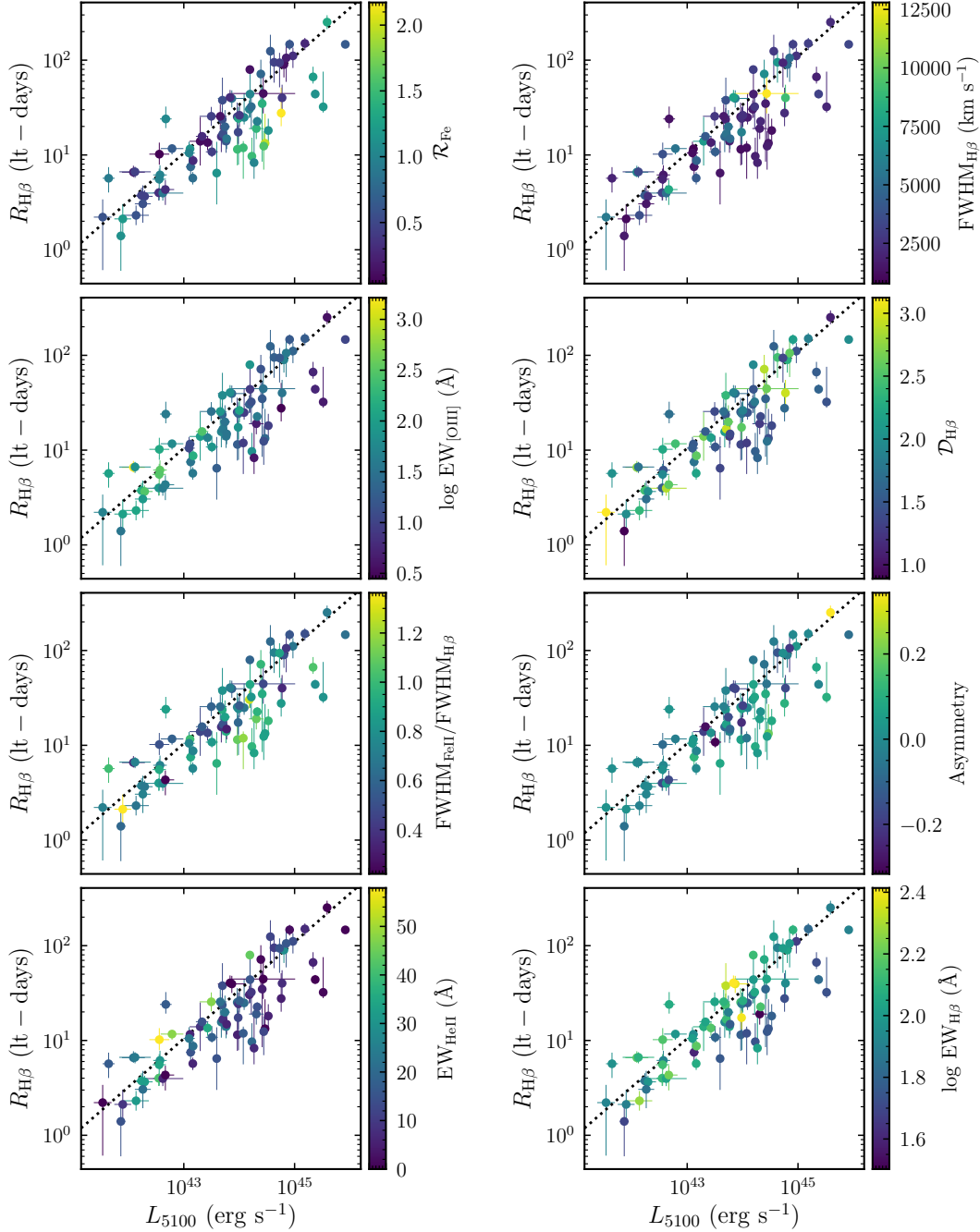


Figure 3. The $R_{\text{H}\beta}$ – L_{5100} relationship color-coded by the spectral properties. The dotted lines are the $R_{\text{H}\beta}$ – L_{5100} relationship for the low-accretion-rate AGNs in Du et al. (2018a). It is obvious that some objects deviate from the dotted lines. The colors show clear trend with \mathcal{R}_{Fe} and $\text{EW}_{\text{H}\beta}$, which means the deviation correlates with \mathcal{R}_{Fe} and $\text{EW}_{\text{H}\beta}$.

metry has been demonstrated using the PG quasar sample in Boroson & Green (1992), and is also associated with the eigenvector 1 sequence. The RM sample reproduces this correlation. Besides, there are some other weak correlations, please see Figure 2. More discussions about the pairwise correlations are provided in Section 4.

3.2. Deviation from the $R_{\text{H}\beta}$ – L_{5100} Relationship

In Figure 3, we first show the $R_{\text{H}\beta}$ – L_{5100} relationship color-coded by the properties we collected. The deviation from the $R_{\text{H}\beta}$ – L_{5100} relationship shows clear correlation with \mathcal{R}_{Fe} and $\text{EW}_{\text{H}\beta}$, both of which show obvious variation trend across the $R_{\text{H}\beta}$ axis in Figure 3. In order to further investigate the significance of the correlations, we define the deviation from the $R_{\text{H}\beta}$ – L_{5100} relationship as

$$\Delta R_{\text{H}\beta} = \log(R_{\text{H}\beta}/R_{\text{H}\beta,\text{R-L}}), \quad (3)$$

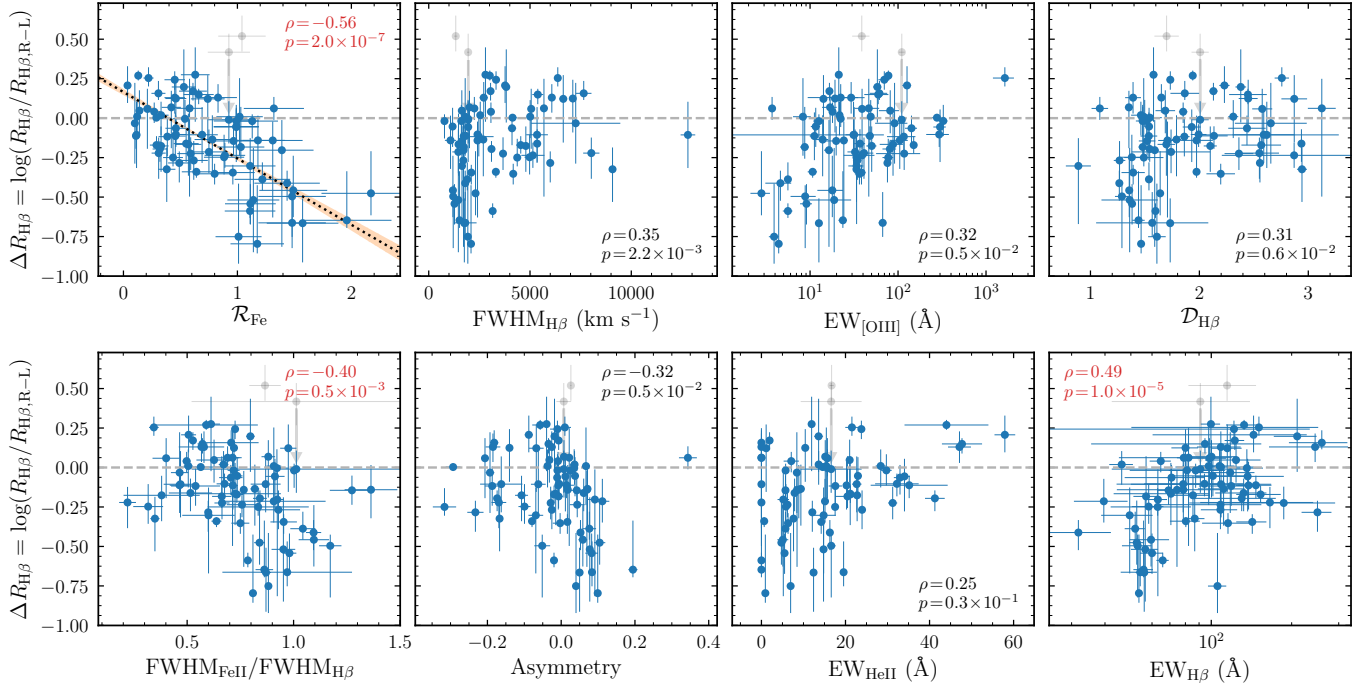


Figure 4. The correlations between $\Delta R_{H\beta}$ and the properties for the sample in the present paper. The Spearman’s rank correlation coefficients (ρ) and the corresponding null probabilities (see Section 3.1) are marked in the corner of each panel (with red color if $p < 0.001$). \mathcal{R}_{Fe} shows significant correlation with $\Delta R_{H\beta}$, and $EW_{H\beta}$ shows a moderate correlation. The grey dashed lines show $\Delta R_{H\beta} = 0$. The black dotted line and the orange color show the linear regression and its confidence band (2σ). The two grey points are MCG +06-26-012 and MCG +06-30-015 (see more details in Section 3.3). We correct the intrinsic reddening MCG +06-30-015 and use its corrected luminosity in the analysis. We do not include MCG +06-26-012 in the analysis.

where $R_{H\beta,R-L}$ is the prediction from the $R_{H\beta}-L_{5100}$ relationship. Here, we adopt $\log R_{H\beta,R-L} = 1.53 + 0.51 \log \ell_{44}$ obtained by Du et al. (2018a) for the AGN with dimensionless accretion rate $\dot{M} < 3$ (\dot{M} is defined by the following Equation (8), please see Section 4.3) as the fiducial $R_{H\beta}-L_{5100}$ relationship. It should be noted that using the $R_{H\beta}-L_{5100}$ relationship in Bentz et al. (2013) doesn’t change the discussion and conclusion in this paper.

The correlations between $\Delta R_{H\beta}$ and the single-epoch properties are shown in Figure 4. Again, the Spearman’s correlation coefficients and the corresponding null probabilities are marked in the corners of the panels in Figure 4. The correlation between $\Delta R_{H\beta}$ and \mathcal{R}_{Fe} is the most significant one. $\Delta R_{H\beta}$ shows a strong anti-correlation with \mathcal{R}_{Fe} with Spearman’s correlation coefficient $\rho = -0.56$ and the null probability $p = 2 \times 10^{-7}$. $\Delta R_{H\beta}$ and $EW_{H\beta}$ shows a weaker correlation with $\rho = 0.49$ and $p = 1 \times 10^{-5}$. In addition, the low- $\mathcal{D}_{H\beta}$ or small- $FWHM_{H\beta}$ objects show more extended distribution of $\Delta R_{H\beta}$, while the high- $\mathcal{D}_{H\beta}$ or large- $FWHM_{H\beta}$ objects have relatively narrower $\Delta R_{H\beta}$ distribution and the average $\Delta R_{H\beta}$ more close to zero. But the Spearman’s coefficients of $\Delta R_{H\beta}$ versus $\mathcal{D}_{H\beta}$ and $FWHM_{H\beta}$ are not high enough. Actually, this complex distribution in the $\Delta R_{H\beta}$ versus $FWHM_{H\beta}$ (or $\mathcal{D}_{H\beta}$) plane may be caused by the eigenvector 1 sequence (the correlation between \mathcal{R}_{Fe} and $FWHM_{H\beta}$, see, e.g., Boroson &

Green 1992; Sulentic et al. 2000; Marziani et al. 2001, 2003; Shen & Ho 2014; Sun, & Shen 2015, or the recent review in Marziani et al. 2018). The large- $FWHM_{H\beta}$ (or high- $\mathcal{D}_{H\beta}$) objects have low \mathcal{R}_{Fe} values, but the small- $FWHM_{H\beta}$ (or low- $\mathcal{D}_{H\beta}$) objects have large range of \mathcal{R}_{Fe} (span from low to high \mathcal{R}_{Fe}). Therefore, the $\Delta R_{H\beta}$ distribution in the small- $FWHM_{H\beta}$ (or low- $\mathcal{D}_{H\beta}$) objects is more extended. Some more discussions about this are provided in Section 4.4. The correlations between $\Delta R_{H\beta}$ and the other parameters are not significant given the present data ($\Delta R_{H\beta}$ shows weak a correlation with $FWHM_{FeII}/FWHM_{H\beta}$). Because the correlation coefficient of \mathcal{R}_{Fe} is the highest among all of the spectral properties, \mathcal{R}_{Fe} can be regarded as the primary parameter that controls the deviation of an AGN from the $R_{H\beta}-L_{5100}$ relationship.

The eigenvector 1 sequence (or main sequence) of AGNs has been extensively investigated in the past decades, and contains the information of the evolution or systematic variation of AGNs (see the recent review in Marziani et al. 2018). Through the analysis of the eigenvector 1 sequence, \mathcal{R}_{Fe} has been demonstrated as a probe of accretion rate/Eddington ratio (e.g., Boroson & Green 1992; Sulentic et al. 2000; Marziani et al. 2001, 2003; Shen & Ho 2014; Sun, & Shen 2015), thus a primary physical driver of the shortened time lags is the accretion rate.

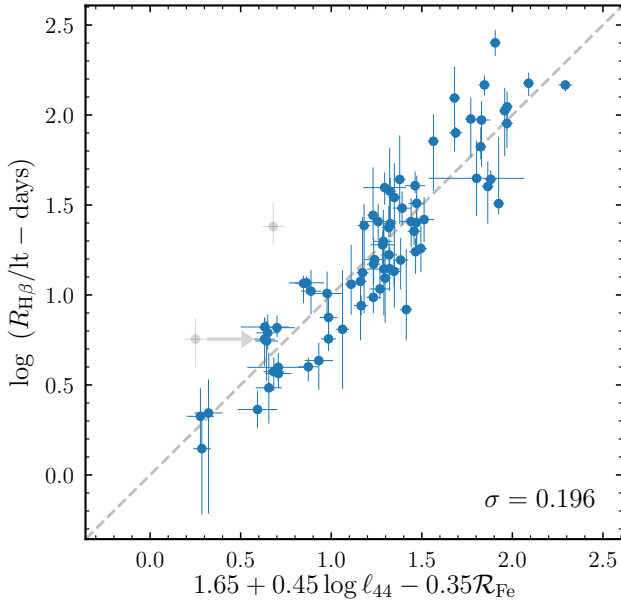


Figure 5. New scaling relation. The scatter of the new scaling relation is $\sigma = 0.196$, and marked in the lower right corner. The two grey points are MCG +06-26-012 and MCG +06-30-015 (see more details in Section 3.3). We correct the intrinsic reddening MCG +06-30-015 and use its corrected luminosity in the analysis. We do not include MCG +06-26-012 in the analysis.

As a simple test, we provide here the linear regression of the correlation between $\Delta R_{H\beta}$ and \mathcal{R}_{Fe} . We adopt the BCES method (Akritas, & Bershady 1996, the orthogonal least squares) to perform the linear regression, which takes into account both of the error bars in x and y axis. MCG +06-26-012 has a relatively low sampling cadence in the first 80 days in its light curve of Wang et al. (2014a) and Hu et al. (2015), which makes its time lag may bias towards longer value. We do not use it in the regression. And the intrinsic reddening of MCG +06-30-015 is strong in light of its high Balmer decrement (Hu et al. 2016). We correct its intrinsic reddening and use the corrected luminosity and the corresponding $R_{H\beta, R-L}$. The MCG +06-26-012 and MCG +06-30-015 are marked as grey points in Figure 4 (also in the following Figure 5). The linear regression is yielded as

$$\Delta R_{H\beta} = -(0.42 \pm 0.06)\mathcal{R}_{Fe} + (0.17 \pm 0.05). \quad (4)$$

The regression and the corresponding confidence band (2σ) are shown in Figure 4. We have also tested that the residual $\Delta R_{H\beta} - \Delta R_{H\beta}(\mathcal{R}_{Fe})$ does not show any correlations with all of the spectral properties (with Spearman’s coefficients $|\rho| < 0.25$), where $\Delta R_{H\beta}(\mathcal{R}_{Fe})$ is the $\Delta R_{H\beta}$ value deduced from \mathcal{R}_{Fe} by Equation (4).

3.3. A New Scaling Relation

Because the strongest correlation is the relation between $\Delta R_{H\beta}$ and \mathcal{R}_{Fe} , we can add \mathcal{R}_{Fe} as a new parameter into the $R_{H\beta}-L_{5100}$ relationship to establish a new scaling relation

with smaller scatter. We fit the RM sample with the following new scaling relation:

$$\log(R_{H\beta}/l_t - \text{days}) = \alpha + \beta \log \ell_{44} + \gamma \mathcal{R}_{Fe}. \quad (5)$$

In order to obtain the uncertainties of the parameters, we employ the bootstrap technique. A subset is generated by resampling N points from the RM sample with replacement (N is the number of the objects in the RM sample). Then, we calculate the best parameters for this subset using the Levenberg-Marquardt method (Press et al. 1992), and repeat this procedure for 5000 times to generate the distributions of α , β , and γ . The final best parameters and the corresponding uncertainties are obtained from the α , β , and γ distributions. The fit is shown in Figure 5, and the best parameters are:

$$\alpha = 1.65 \pm 0.06, \beta = 0.45 \pm 0.03, \gamma = -0.35 \pm 0.08. \quad (6)$$

The scatter of the new scaling relation is $\sigma = 0.196$, which is much smaller than the original scatter of the $R_{H\beta}-L_{5100}$ relationship ($\sigma \sim 0.28$, see Du et al. 2018a).

4. DISCUSSIONS

4.1. Some Discussions on Pairwise Correlations

In Section 3.1, we showed the pairwise correlations between the parameters we compiled. Some of the correlations have been presented in the literatures using different samples of AGNs, and some have been discussed directly or indirectly. A $\sigma_{H\beta}-\mathcal{D}_{H\beta}$ correlation, which is a width-profile correlation of the H β line similar to the $\text{FWHM}_{H\beta}-\mathcal{D}_{H\beta}$ in this paper, was presented in Collin et al. (2006) using the RM sample at that time. It was also discussed by Kollatschny & Zetzl (2011, 2013) and explained as the different contributions from the rotation/Keplerian motions and the turbulent velocities in the objects with different line widths (Kollatschny & Zetzl 2011, 2013). The correlation in Figure 2 is generally the same as in Kollatschny & Zetzl (2011), but has more objects at the narrow-width (small $\text{FWHM}_{H\beta}$) end because the current sample has more NLS1s or high-accretion-rate objects. However, it should be noted that the parameter $\mathcal{D}_{H\beta}$ involves $\text{FWHM}_{H\beta}$ as the numerator, thus may introduce a certain degree of self correlation to the $\text{FWHM}_{H\beta}-\mathcal{D}_{H\beta}$ relation.

The comparison between $\text{FWHM}_{Fe II}$ and $\text{FWHM}_{H\beta}$ has been presented for the quasar sample in the Sloan Digital Sky Survey (SDSS) in, e.g., Hu et al. (2008a,b); Cracco et al. (2016). The $\text{FWHM}_{Fe II}$ is systematically smaller than $\text{FWHM}_{H\beta}$, which was demonstrated and explained by the contribution from an intermediate-line region in Hu et al. (2008a,b). The Fe II emission and the intermediate-width component of H β line are both from this intermediate-line region, and H β has an extra very broad component (Hu et al. 2008a,b). In addition, Hu et al. (2015) shows a comparison between the time lags of Fe II and H β using the SEAMBH sample, which is also a direct evidence for the relatively larger size of Fe II-emitting region and the smaller H β -emitting region. And Hu et al. (2015) also shows that

the lag ratio between Fe II and H β correlates with \mathcal{R}_{Fe} . The $\mathcal{R}_{\text{Fe}} - \text{FWHM}_{\text{Fe II}}/\text{FWHM}_{\text{H}\beta}$ correlation in Figure 2 may have the same physical origin as the correlation between the lag ratio and \mathcal{R}_{Fe} (The gas in the Fe II region has a larger size and a smaller FWHM). Similarly, FWHM $_{\text{H}\beta}$ correlates with FWHM $_{\text{Fe II}}/\text{FWHM}_{\text{H}\beta}$ (see in Figure 2) because of the $\mathcal{R}_{\text{Fe}} - \text{FWHM}_{\text{H}\beta}$ correlation (Eigenvector 1 sequence, e.g., Boroson & Green 1992; Sulentic et al. 2000; Marziani et al. 2001, 2003, 2018; Shen & Ho 2014).

The principal component analysis in Boroson & Green (1992) has shown a weak correlation between \mathcal{R}_{Fe} and EW $_{\text{H}\beta}$ using the PG quasar sample, however with a relatively small correlation coefficient of -0.425 (see more details in Boroson & Green 1992). The \mathcal{R}_{Fe} and EW $_{\text{H}\beta}$ of the RM sample presented in this paper show a slightly stronger correlation with Spearman’s coefficient of $\rho = -0.60$. This correlation may be related to the Baldwin effect of H β line (e.g., Baldwin 1977; Korista, & Goad 2004), and especially with the intrinsic Baldwin effect (e.g., Gilbert, & Peterson 2003; Rakić et al. 2017). The intrinsic Baldwin effect shows an anti-correlation between EW of the emission line and the luminosity, and is also equivalent to an anti-correlation between EW and the accretion rate because the BH mass keeps a constant during the observation campaign (e.g., Gilbert, & Peterson 2003; Rakić et al. 2017). The \mathcal{R}_{Fe} parameter is correlated with Eddington ratio/accretion rate, thus is naturally correlated with the EW $_{\text{H}\beta}$.

The asymmetry- \mathcal{R}_{Fe} correlation has been shown in Boroson & Green (1992), and discussed in the context of eigenvector 1 sequence (Sulentic et al. 2002). The high- \mathcal{R}_{Fe} objects tend to have stronger blue H β wings, and vice versa. The FWHM $_{\text{Fe II}}/\text{FWHM}_{\text{H}\beta}$ -asymmetry and FWHM $_{\text{H}\beta}$ -asymmetry correlations can also attribute to the asymmetry- \mathcal{R}_{Fe} correlation. The origin of the H β asymmetry must be subject to the geometry and kinematics of the BLRs, but is still under some debate because of the degeneracy of H β profiles with different BLR geometry and kinematics. A recent dedicated RM campaign project for the BLR kinematics of the AGNs with H β asymmetry⁴ has started (Du et al. 2018b), and may provide more observations for the velocity-resolved RM measurements in the future.

The EW $_{[\text{O III}]}$ -EW $_{\text{He II}}$ correlation is a natural result of the photoionization physics. Both of [O III] and He II have high ionization energy (54.9 eV for [O III] and 54.4 eV for He II, respectively), thus are sensitive to the variation of the AGN circumstances (e.g., spectral energy distribution, SED) in a similar way.

4.2. The New Scaling Relation and BH Mass Measurement

Through the analysis in this paper, we found that the \mathcal{R}_{Fe} parameter is the dominant observational property in the scatter of the $R_{\text{H}\beta} - L_{5100}$ relationship. This confirms the state-

⁴ They may have some special BLR kinematics or inhomogeneous gas distribution, or even binary BHs in their centers (see more details in Du et al. 2018b).

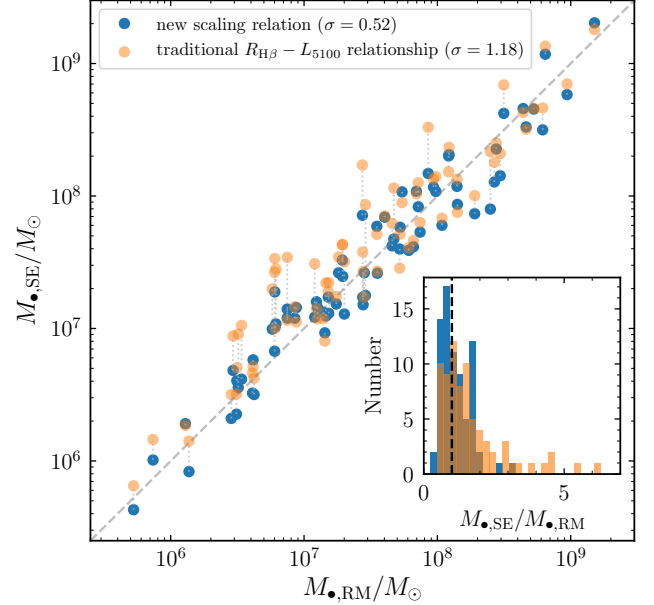


Figure 6. Single-epoch BH mass versus RM BH mass. The blue points are estimated by the new scaling relation, while the orange points are obtained by the traditional $R_{\text{H}\beta} - L_{5100}$ relationship. The embedded panel shows the distributions of $M_{\bullet, \text{SE}}/M_{\bullet, \text{RM}}$ of the new scaling relation and the $R_{\text{H}\beta} - L_{5100}$ relationship. The BH masses estimated by the $R_{\text{H}\beta} - L_{5100}$ relationship are biased towards to higher values with respect to those from the new scaling relation. The standard deviations (simply denoted by σ) of the distributions are provided in the upper-left corner. We do not plot the error bars in order to show the differences more clearly.

ment that the AGNs with high accretion rates tend to have shortened lags in Du et al. (2015, 2016a, 2018a). The shortened time lags in high- \mathcal{R}_{Fe} /high-accretion-rate AGNs imply smaller BLR scale sizes and smaller BH mass estimates with respect to the traditional $R_{\text{H}\beta} - L_{5100}$ relationship.

The $R_{\text{H}\beta} - L_{5100}$ relationship was heavily utilized as a single-epoch BH mass estimator in large AGN samples, and helped establish our paradigm for AGN evolution (McLure & Dunlop 2004; Vestergaard & Peterson 2006; Kollmeier et al. 2006; Greene & Ho 2007; Shen et al. 2011). The shortened time lags in high- \mathcal{R}_{Fe} /high-accretion-rate AGNs make it vital to take this into account in the BH mass estimation. Therefore, we suggest calculate the BH masses from single-epoch spectra following the steps below: (1) obtain the $R_{\text{H}\beta}$ from the luminosities and the strength of Fe II (\mathcal{R}_{Fe}) using Equation (5), (2) get the BH mass by the following Equation (7) from the line width and the estimated $R_{\text{H}\beta}$. Then, the dimensionless accretion rate can be easily estimated by the following Equation (8) in Section 4.3.

In combination with the velocity width (ΔV) of the emission line, RM measurement yields an estimate of BH mass as

$$M_{\bullet} = f_{\text{BLR}} \frac{\Delta V^2 R_{\text{BLR}}}{G} \quad (7)$$

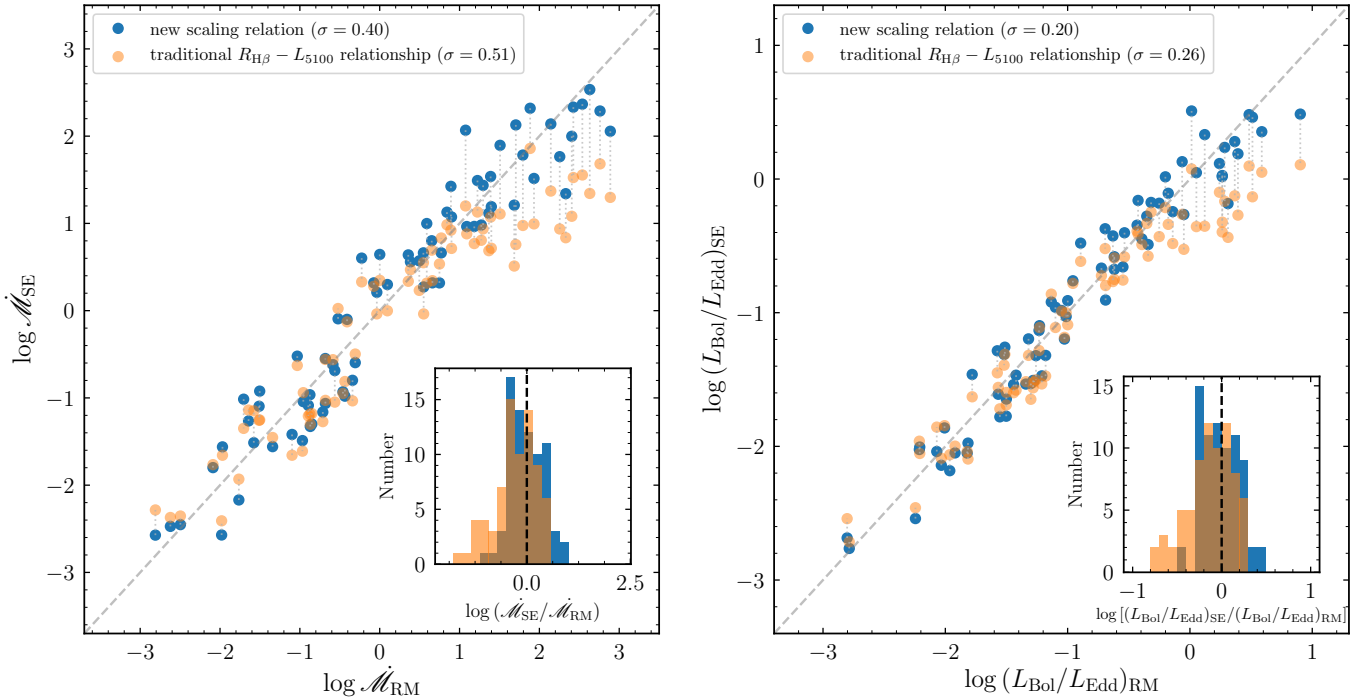


Figure 7. Accretion rates and Eddington ratios from the single-epoch spectra and the RM observations. The blue points are deduced by the new scaling relation, while the orange points are obtained by the $R_{\text{H}\beta}$ – L_{5100} relationship. The embedded panel shows the corresponding distributions of $\log(\dot{M}_{\text{SE}}/\dot{M}_{\text{RM}})$ and $\log[(L_{\text{Bol}}/L_{\text{Edd}})_{\text{SE}}/(L_{\text{Bol}}/L_{\text{Edd}})_{\text{RM}}]$. The accretion rates and Eddington ratios estimated from the $R_{\text{H}\beta}$ – L_{5100} relationship are biased downward in the high- \dot{M} end. The standard deviations (simply denoted by σ) of the distributions are provided in the upper-left corner. We do not plot the error bars in order to show the differences more clearly.

(e.g., Wandel et al. 1999; Peterson & Wandel 1999; Peterson et al. 2004), where G is the gravitational constant, and f_{BLR} is the virial factor related to the geometry and kinematics of the BLR (e.g., Onken et al. 2004; Park et al. 2012; Grier et al. 2013a; Ho & Kim 2014; Woo et al. 2015). Although measuring BH mass through RM technique is feasible for a small number of objects, it is not easy to apply RM to large AGN samples because RM is fairly time-consuming (always continuing for months to years). Some multi-object RM campaigns based on fiber-fed telescopes, e.g., the RM campaigns of SDSS (Shen et al. 2015) and OZDES (King et al. 2015), are committed to enlarge the sample of RM objects but still ongoing. Fortunately, the $R_{\text{H}\beta}$ – L_{5100} relationship can be used to obtain R_{BLR} from the single-epoch spectra very simply.

The geometry and kinematics of the BLRs determine the virial factor f_{BLR} in BH mass estimate (in Equation 7). Comparing the RM AGNs with stellar velocity dispersion measurements with M_{\bullet} – σ_{\star} relation of inactive galaxies gives $f_{\text{BLR}} \sim 1$ if the velocity width of $\text{H}\beta$ is measured from $\text{FWHM}_{\text{H}\beta}$ (e.g., Onken et al. 2004; Ho & Kim 2014; Woo et al. 2015). The virial factor for high- \mathcal{R}_{Fe} /high-accretion-rate AGNs is still a matter of some debate. Through fitting AGN spectral energy distribution by accretion disk model, Mejía-Restrepo et al. (2018) found a correlation between the virial factor and the width of emission line ($f_{\text{BLR}} \sim 3$ if $\text{FWHM}_{\text{H}\beta} \sim 1500 \text{ km s}^{-1}$ and $f_{\text{BLR}} \sim 0.4$ if $\text{FWHM}_{\text{H}\beta} \sim 10000 \text{ km s}^{-1}$). Yu et al. (2019) also shows potential a corre-

lation between f_{BLR} and line width. From the BLR modeling results of the small samples in Pancoast et al. (2014); Grier et al. (2017b); Williams et al. (2018), the virial factor is roughly consistent with the value derived from the M_{\bullet} – σ_{\star} relation, and the virial factors of individual objects do not show significant correlation with the Eddington ratios (or show potential and weak anti-correlation, namely smaller virial factor for higher Eddington ratio). NLS1s (thought to have smaller BH masses and higher accretion rates) tend to host pseudobulges (e.g., Mathur et al. 2012). Ho & Kim (2014) classified the AGN sample to classical bulges/ellipticals and pseudobulges, and derived a virial factor of the AGNs with pseudobulges smaller than 1. Woo et al. (2015) found that NLS1s have no significant differences from the other AGNs, and derived $f_{\text{BLR}} = 1.12$ if using $\text{FWHM}_{\text{H}\beta}$ as the line-width measurement. Thus, adopting $f_{\text{BLR}} \sim 1$ and acknowledging its large uncertainty is acceptable at present.

As a simple test, we compare the BH masses measured by RM ($M_{\bullet,\text{RM}}$) with the masses estimated from the single-epoch spectra ($M_{\bullet,\text{SE}}$) using both of the new scaling relation in Section 3.3 and the traditional $R_{\text{H}\beta}$ – L_{5100} relationship (see Section 3.2) in Figure 6. Here, we adopt $f_{\text{BLR}} = 1$ for simplicity and list the RM BH masses in Table 1. The scatter is quantified by the standard deviation of $M_{\bullet,\text{SE}}/M_{\bullet,\text{RM}}$. We do not plot the error bars in order to show clearly the differences between the estimates from the new scaling relation and the $R_{\text{H}\beta}$ – L_{5100} relationship. The scatter of $M_{\bullet,\text{SE}}$

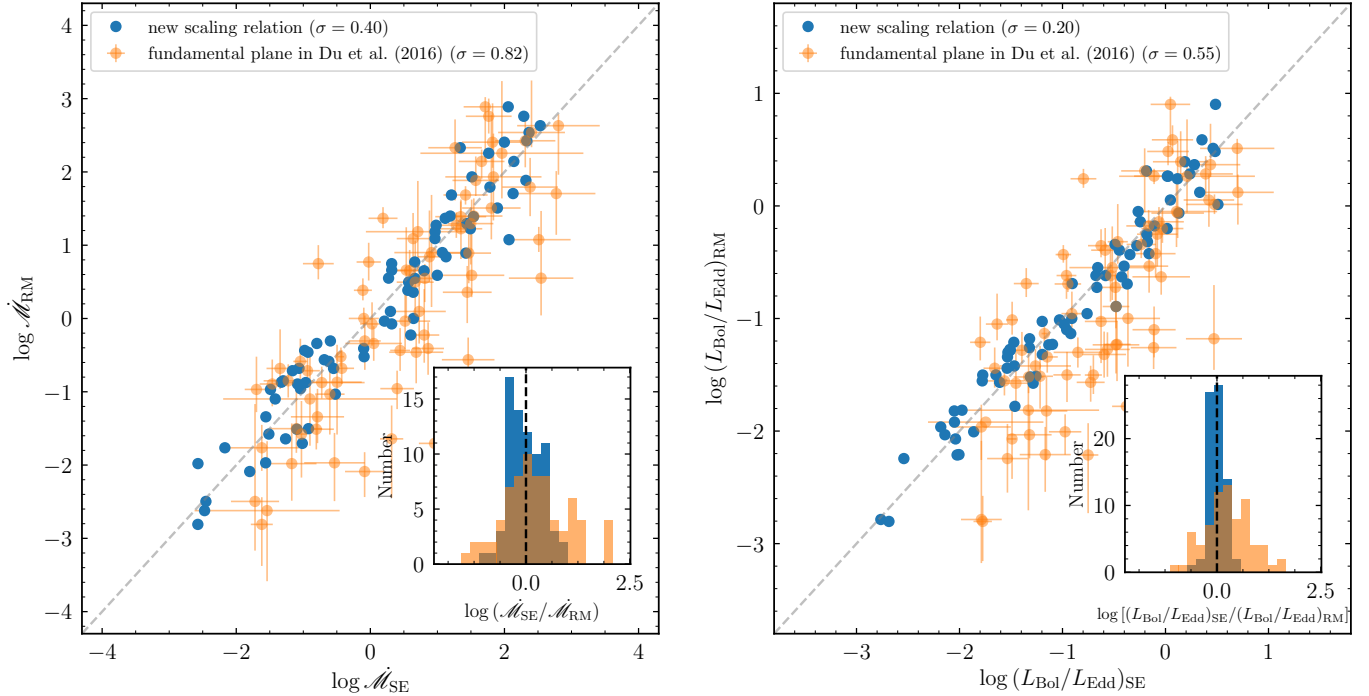


Figure 8. Comparisons with the accretion rates and Eddington ratios estimated from the fundamental plane of BLR. The blue points are deduced by the new scaling relation, while the orange points are obtained by the FP in Du et al. (2016b). The embedded panel shows the corresponding distributions of $\log(\dot{M}_{\text{SE}}/\dot{M}_{\text{RM}})$ and $\log[(L_{\text{Bol}}/L_{\text{Edd}})_{\text{SE}}/(L_{\text{Bol}}/L_{\text{Edd}})_{\text{RM}}]$. The accretion rates and Eddington ratios estimated from the FP show much larger scatter. The standard deviations (simply denoted by σ) of the distributions are provided in the upper-left corner. We do not plot the error bars of the blue points for clarity.

from the new scaling relation is 0.52, while the scatter obtained by the traditional $R_{\text{H}\beta}$ - L_{5100} relationship is 1.18. The embedded plot in Figure 6 shows the distributions of $M_{\bullet,\text{SE}}/M_{\bullet,\text{RM}}$. The $M_{\bullet,\text{SE}}/M_{\bullet,\text{RM}}$ distribution is biased toward the value larger than 1 for the traditional $R_{\text{H}\beta}$ - L_{5100} relationship, which means the BH masses are overestimated if using this simple relationship.

Recently, Martínez-Aldama et al. (2019) found a correction for the time delay based on the dimensionless accretion rate (\dot{M} in the following Section 4.3) considering the anticorrelation between f_{BLR} and line width, established a correlation between the corrected time lag ($R_{\text{BLR}}^{\text{corr}}$) and L_{5100} , and discussed the measurements of the cosmological distances using this correlation. Their correction ($R_{\text{BLR}}^{\text{corr}}$) relies on the measured L_{5100} , $\text{FWHM}_{\text{H}\beta}$, and R_{BLR} itself. The new scaling relation in the present paper is established in a different perspective (based on spectral properties), and can deduce R_{BLR} directly from L_{5100} and \mathcal{R}_{Fe} .

4.3. Accretion Rate and Eddington Ratio

Because of the shortened lags, the accretion rates or Eddington ratios would be underestimated by factors of a few if using the traditional $R_{\text{H}\beta}$ - L_{5100} relationship. From the standard disk model (Shakura, & Sunyaev 1973), the accretion rate can be estimated by the formula of

$$\dot{M} = 20.1 \left(\frac{\ell_{44}}{\cos i} \right)^{3/2} m_7^{-2}, \quad (8)$$

where $m_7 = M_{\bullet}/10^7 M_{\odot}$, and i is inclination angle of the accretion disk (here we adopt $\cos i = 0.75$ as an average value for all of the AGNs, see the discussions in Du et al. 2014; Wang et al. 2014a; Du et al. 2016a). Here, we compare the \dot{M} and Eddington ratio ($L_{\text{Bol}}/L_{\text{Edd}}$) estimates obtained from the single-epoch spectra (using the new scaling relation and the $R_{\text{H}\beta}$ - L_{5100} relationship) with those values calculated from RM (listed in Table 1) in Figure 7, where L_{Bol} is the bolometric luminosity and $L_{\text{Edd}} = 1.5 \times 10^{38} (M_{\bullet}/M_{\odot})$ is the Eddington luminosity for the gas with solar composition. Here we simply adopt $L_{\text{Bol}} = 10 L_{5100}$ (Kaspi et al. 2000), but it should be noted that the bolometric correction factor depends on accretion rate or BH mass (Jin et al. 2012). We do not draw the error bars in order to show the differences at high- \dot{M} end more clearly. It is obvious that the points of the new scaling relation at high-accretion-rate end are much closer to the diagonal, while those estimated by the traditional $R_{\text{H}\beta}$ - L_{5100} relationship are biased downward. The distributions and the standard deviations of $\log(\dot{M}_{\text{SE}}/\dot{M}_{\text{RM}})$ and $\log[(L_{\text{Bol}}/L_{\text{Edd}})_{\text{SE}}/(L_{\text{Bol}}/L_{\text{Edd}})_{\text{RM}}]$ are also provided in Figure 7. The new scaling relation should be preferentially used in the estimation of accretion rates or Eddington ratios from the single-epoch spectra in the statistical study of large AGN samples.

Du et al. (2016b) established a bivariate correlation between \dot{M} and $(\mathcal{R}_{\text{Fe}}, \mathcal{D}_{\text{H}\beta})$, which can be used to estimate

the accretion rate directly from the BLR properties. It is called the fundamental plane (FP) of BLR. The FP can deduce \dot{M} or Eddington ratio estimates without any luminosity measurements (see also Negrete et al. 2018), however has fairly large uncertainties (the scatter of the FP is 0.7 for \dot{M} and 0.48 for Eddington ratio, respectively, see more details in Du et al. 2016b). As a comparison, we plot the \dot{M} estimates from the FP and the new scaling relation in Figure 8. The single-epoch \dot{M} and Eddington ratios corresponding to the FP method are estimated from the \mathcal{R}_{Fe} and $\mathcal{D}_{\text{H}\beta}$ listed in Table 2 and the FP in Du et al. (2016b). It should be noted that we switch x and y axes of Figure 8 (with respect to Figure 7) for easier comparison with the figures in Du et al. (2016b). Again, we do not draw the error bars of the \dot{M} from the new scaling relation for clarity. The scatters of the \dot{M} and $L_{\text{Bol}}/L_{\text{Edd}}$ estimated from the FP are much larger. The FP connect the BLR physics with the accretion status of AGNs, however the different temperature, number density, metallicity of the BLR in different AGN introduces large uncertainties. The FP (Du et al. 2016b) is a good beginning that searches for direct indicator of accretion rate from the BLR observational properties, but its scatter and accuracy should be improved by including more observational properties in the future.

The strong correlation between accretion rates \dot{M} and \mathcal{R}_{Fe} has been explored by Panda et al. (2018, 2019), but still remains open. Accretion flows to the central BHs supplied by either star formation from torus (Wang et al. 2010), or asymmetric dynamics (Begelman, & Shlosman 2009) will have different dependence on metallicity, however, \mathcal{R}_{Fe} is not a unique function of metallicity (Baldwin et al. 2004; Verner et al. 2004). More details of photoionization are necessary to investigate \mathcal{R}_{Fe} dependence on BLR clouds (density, temperature and metallicity) and the SEDs of accretion disks.

4.4. Accretion Rate or Orientation?

The eigenvector 1 sequence can do some help to break the degeneracy of accretion rate and orientation. It was demonstrated that the accretion rate or Eddington ratio drives the variation of \mathcal{R}_{Fe} , while the orientation effect dominantly controls the dispersion in $\text{FWHM}_{\text{H}\beta}$ at fixed \mathcal{R}_{Fe} (e.g., Marziani et al. 2001; Shen & Ho 2014). We plot the eigenvector 1 sequence of the RM sample color-coded by $\Delta R_{\text{H}\beta}$ in Figure 9. It is obvious that the objects with the most significant lag deviations are located in the lower right corner (with the strongest \mathcal{R}_{Fe}). Furthermore, there is no significant trend in the $\text{FWHM}_{\text{H}\beta}$ -axis at fixed \mathcal{R}_{Fe} . It means that the accretion rate definitely plays the primary role in the shortening of the time lags but the orientation does not contribute much. In Figure 4, the dispersion of the $\Delta R_{\text{H}\beta}$ at lower $\text{FWHM}_{\text{H}\beta}$ is larger, this is caused by the higher \mathcal{R}_{Fe} in those objects, which is clearly shown in Figure 9.

5. SUMMARY

In this paper, we systematically investigate the dependence of the $R_{\text{H}\beta}$ - L_{5100} relationship on optical spectra for a wide

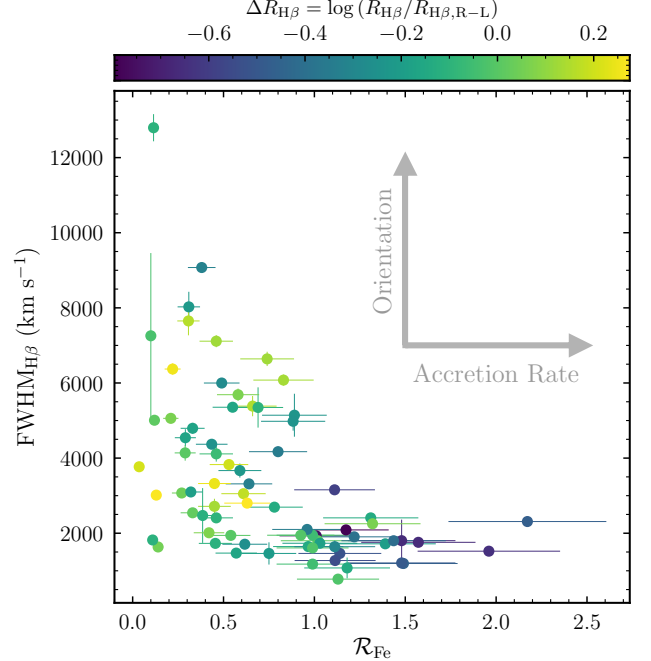


Figure 9. Main Sequence of AGNs. The points are color-coded by $\Delta R_{\text{H}\beta}$. Accretion rate/Eddington ratio drives the variation of \mathcal{R}_{Fe} , while the orientation effect dominantly controls the dispersion in $\text{FWHM}_{\text{H}\beta}$ at fixed \mathcal{R}_{Fe} (Marziani et al. 2001; Shen & Ho 2014). It is obvious that accretion rate definitely plays the primary role in the shortening of the time lags (see more details in Section 4.4).

range of AGN parameters. The reverberation mapping campaign of the AGNs with high accretion rates show many objects deviate significantly from the traditional $R_{\text{H}\beta}$ - L_{5100} relationship (Du et al. 2015, 2016a, 2018a). We collect 8 different single-epoch spectral properties to investigate how the deviation of an AGN from the $R_{\text{H}\beta}$ - L_{5100} relationship correlates with those properties and to understand what is the origin of the shortened lags.

- The flux ratio between Fe II and H β lines (\mathcal{R}_{Fe}) is confirmed to be the most prominent property that correlates with the deviation of an AGN from the $R_{\text{H}\beta}$ - L_{5100} relationship. \mathcal{R}_{Fe} is thought to be the indicator of accretion rate, therefore, accretion rate is the driver for the shortened lags. $\text{FWHM}_{\text{H}\beta}$, which is induced by the orientation of an AGN to line of sight, does not show clear trend with the lag shortening. Thus, the orientation is not a dominant factor.
- We established a new scaling relation with the form of $\log R_{\text{H}\beta} = \alpha + \beta \log \ell_{44} + \gamma \mathcal{R}_{\text{Fe}}$, which can be used as a single-epoch estimator of BH mass and accretion rate, where $\alpha = 1.65 \pm 0.06$, $\beta = 0.45 \pm 0.03$, and $\gamma = -0.35 \pm 0.08$. The scatter of the new scaling relation is 0.196.

The new scaling relation provides an empirical relation of the BLR regions with optical spectra. It is less biased and

provides more robust estimates of the BH mass and accretion rate/Eddington ratio.

JMW is grateful to all members of the SEAMBH project for great efforts since 2012. In particular, the continuous supports from the Lijiang 2.4m telescope of Yunnan Observatories is acknowledged as well as staff's operation.

Funding for the telescope has been provided by CAS and the People's Government of Yunnan Province. We acknowledge the support by National Key R&D Program of China (2016YFA0400701), by NSFC through grants NSFC-11873048, 11833008, 11690024, and by grant No. QYZDJ-SSW-SLH007 from the Key Research Program of Frontier Sciences, CAS, by the Strategic Priority Research Program of the Chinese Academy of Sciences grant No. XDB23010400.

REFERENCES

- Akritas, M. G., & Bershad, M. A. 1996, *ApJ*, 470, 706
- Bahcall, J. N., Kozlovsky, B.-Z., & Salpeter, E. E. 1972, *ApJ*, 171, 467
- Baldwin, J. A. 1977, *ApJ*, 214, 679
- Baldwin, J. A., Ferland, G. J., Korista, K. T., et al. 2004, *ApJ*, 615, 610
- Barth, A. J., Bennert, V. N., Canalizo, G., et al. 2015, *ApJS*, 217, 26
- Barth, A. J., Pancoast, A., Bennert, V. N., et al. 2013, *ApJ*, 769, 128
- Barth, A. J., Pancoast, A., Thorman, S. J., et al. 2011, *ApJ*, 743, 4
- Begelman, M. C., & Shlosman, I. 2009, *ApJL*, 702, L5
- Bentz, M. C., Denney, K. D., Grier, C. J., et al. 2013, *ApJ*, 767, 149
- Bentz, M. C., Horenstein, D., Bazhaw, C., et al. 2014, *ApJ*, 796, 8
- Bentz, M. C., Denney, K. D., Cackett, E. M., et al. 2007, *ApJ*, 662, 205
- Bentz, M. C., Walsh, J. L., Barth, A. J., et al. 2008, *ApJ*, 689, L21
- Bentz, M. C., Denney, K. D., Cackett, E. M., et al. 2006, *ApJ*, 651, 775
- Bentz, M. C., Walsh, J. L., Barth, A. J., et al. 2009a, *ApJ*, 705, 199
- Bentz, M. C., Peterson, B. M., Netzer, H., Pogge, R. W., & Vestergaard, M. 2009b, *ApJ*, 697, 160
- Bentz, M. C., Batista, M., Seals, J., et al. 2016a, *ApJ*, 831, 2
- Bentz, M. C., Cackett, E. M., Crenshaw, D. M., et al. 2016b, *ApJ*, 830, 136
- Bian, W.-H., Huang, K., Hu, C., et al. 2010, *ApJ*, 718, 460
- Blandford, R. D., & McKee, C. F. 1982, *ApJ*, 255, 419
- Boroson, T. A., & Green, R. F. 1992, *ApJS*, 80, 109
- Brotherton, M. S. 1996, *ApJS*, 102, 1
- Brotherton, M. S., Du, P., Bao, D.-W., et al. 2019, in prep.
- Bruzual, G., & Charlot, S. 2003, *MNRAS*, 344, 1000
- Cackett, E. M., Chiang, C.-Y., McHardy, I., et al. 2018, *ApJ*, 857, 53
- Collin, S., Kawaguchi, T., Peterson, B. M., et al. 2006, *A&A*, 456, 75
- Cracco, V., Ciroi, S., Berton, M., et al. 2016, *MNRAS*, 462, 1256
- Czerny, B., Wang, J.-M., Du, P., et al. 2019, *ApJ*, 870, 84
- Denney, K. D., Bentz, M. C., Peterson, B. M., et al. 2006, *ApJ*, 653, 152
- Denney, K. D., Peterson, B. M., Pogge, R. W., et al. 2009, *ApJ*, 704, L80
- Denney, K. D., Peterson, B. M., Pogge, R. W., et al. 2010, *ApJ*, 721, 715
- De Robertis, M. 1985, *ApJ*, 289, 67
- De Rosa, G., Fausnaugh, M. M., Grier, C. J., et al. 2018, *ApJ*, 866, 133
- Dietrich, M., Peterson, B. M., Albrecht, P., et al. 1998, *ApJS*, 115, 185
- Dietrich, M., Peterson, B. M., Grier, C. J., et al. 2012, *ApJ*, 757, 53
- Doroshenko, V. T., Sergeev, S. G., & Pronik, V. I. 2008, *Astronomy Reports*, 52, 442
- Du, P., Hu, C., Lu, K.-X., et al. 2014, *ApJ*, 782, 45
- Du, P., Hu, C., Lu, K.-X., et al. 2015, *ApJ*, 806, 22
- Du, P., Lu, K.-X., Zhang, Z.-X., et al. 2016a, *ApJ*, 825, 126
- Du, P., Wang, J.-M., Hu, C., et al. 2016b, *ApJ*, 818, L14
- Du, P., Zhang, Z.-X., Wang, K., et al. 2018a, *ApJ*, 856, 6
- Du, P., Brotherton, M. S., Wang, K., et al. 2018b, *ApJ*, 869, 142
- Edelson, R., Gelbord, J. M., Horne, K., et al. 2015, *ApJ*, 806, 129
- Fausnaugh, M. M., Grier, C. J., Bentz, M. C., et al. 2017, *ApJ*, 840, 97
- Gilbert, K. M., & Peterson, B. M. 2003, *ApJ*, 587, 123
- Greene, J. E., & Ho, L. C. 2007, *ApJ*, 667, 131
- Grier, C. J., Martini, P., Watson, L. C., et al. 2013a, *ApJ*, 773, 90
- Grier, C. J., Peterson, B. M., Pogge, R. W., et al. 2012, *ApJ*, 755, 60
- Grier, C. J., Trump, J. R., Shen, Y., et al. 2017b, *ApJ*, 851, 21
- Grier, C. J., Shen, Y., Horne, K., et al. 2019, *arXiv:1904.03199*
- Ho, L. C., Filippenko, A. V., & Sargent, W. L. 1995, *ApJS*, 98, 477
- Ho, L. C., & Kim, M. 2014, *ApJ*, 789, 17
- Hu, C., Wang, J.-M., Ho, L. C., et al. 2008a, *ApJ*, 683, L115
- Hu, C., Wang, J.-M., Ho, L. C., et al. 2008b, *ApJ*, 687, 78
- Hu, C., Du, P., Lu, K.-X., et al. 2015, *ApJ*, 804, 138
- Hu, C., Wang, J.-M., Ho, L. C., et al. 2016, *ApJ*, 832, 197
- Hu, C., Du, P., Guo, W.-J., et al. 2019, in prep.
- Ilić, D., Popović, L. Č., Bon, E., et al. 2006, *MNRAS*, 371, 1610
- Jin, C., Ward, M., & Done, C. 2012, *MNRAS*, 425, 907
- Jones, D. H., Read, M. A., Saunders, W., et al. 2009, *MNRAS*, 399, 683
- Kaspi, S., Brandt, W. N., Maoz, D., et al. 2007, *ApJ*, 659, 997

- Kaspi, S., Maoz, D., Netzer, H., et al. 2005, *ApJ*, 629, 61
- Kaspi, S., Smith, P. S., Netzer, H., et al. 2000, *ApJ*, 533, 631
- Kewley, L. J., Groves, B., Kauffmann, G., & Heckman, T. 2006, *MNRAS*, 372, 961
- Kim, D.-C., Sanders, D. B., Veilleux, S., et al. 1995, *ApJS*, 98, 129
- King, A. L., Martini, P., Davis, T. M., et al. 2015, *MNRAS*, 453, 1701
- Kollatschny, W., & Zetzl, M. 2011, *Nature*, 470, 366
- Kollatschny, W., & Zetzl, M. 2013, *A&A*, 549, A100
- Kollmeier, J. A., Onken, C. A., Kochanek, C. S., et al. 2006, *ApJ*, 648, 128
- Korista, K. T., & Goad, M. R. 2004, *ApJ*, 606, 749
- Lu, K.-X., Du, P., Hu, C., et al. 2016, *ApJ*, 827, 118
- Mathur, S., Fields, D., Peterson, B. M., et al. 2012, *ApJ*, 754, 146
- Martínez-Aldama, M., Czerny, B., Kawka, D., et al. 2019, arXiv:1903.09687
- Marziani, P., Dultzin, D., Sulentic, J. W., et al. 2018, *Frontiers in Astronomy and Space Sciences*, 5, 6
- Marziani, P., Sulentic, J. W., Zwitter, T., Dultzin-Hacyan, D., & Calvani, M. 2001, *ApJ*, 558, 553
- Marziani, P., Zamanov, R. K., Sulentic, J. W., & Calvani, M. 2003, *MNRAS*, 345, 1133
- McHardy, I. M., Connolly, S. D., Horne, K., et al. 2018, *MNRAS*, 480, 2881
- McLure, R. J., & Dunlop, J. S. 2004, *MNRAS*, 352, 1390
- Mejía-Restrepo, J. E., Lira, P., Netzer, H., et al. 2018, *Nature Astronomy*, 2, 63
- Moustakas, J., & Kennicutt, R. C. 2006, *ApJS*, 164, 81
- Negrete, C. A., Dultzin, D., Marziani, P., et al. 2018, *A&A*, 620, A118
- Onken, C. A., Ferrarese, L., Merritt, D., et al. 2004, *ApJ*, 615, 645
- Osterbrock, D. E., & Ferland, G. J. 2006, *Astrophysics of gaseous nebulae and active galactic nuclei*, 2nd. ed. by D.E. Osterbrock and G.J. Ferland. Sausalito, CA: University Science Books, 2006,
- Pancoast, A., Brewer, B. J., Treu, T., et al. 2014, *MNRAS*, 445, 3073
- Panda, S., Czerny, B., Adhikari, T. P., et al. 2018, *ApJ*, 866, 115
- Panda, S., Marziani, P., & Czerny, B. 2019, arXiv:1905.01729
- Rakić, N., La Mura, G., Ilić, D., et al. 2017, *A&A*, 603, A49
- Park, D., Kelly, B. C., Woo, J.-H., & Treu, T. 2012, *ApJS*, 203, 6
- Pei, L., Barth, A. J., Aldering, G. S., et al. 2014, *ApJ*, 795, 38
- Pei, L., Fausnaugh, M. M., Barth, A. J., et al. 2017, *ApJ*, 837, 131
- Peterson, B. M., Ali, B., Horne, K., et al. 1993, *PASP*, 105, 247
- Peterson, B. M., Berlind, P., Bertram, R., et al. 2002, *ApJ*, 581, 197
- Peterson, B. M., Ferrarese, L., Gilbert, K. M., et al. 2004, *ApJ*, 613, 682
- Peterson, B. M., Grier, C. J., Horne, K., et al. 2014, *ApJ*, 795, 149
- Peterson, B. M., & Wandel, A. 1999, *ApJL*, 521, L95
- Peterson, B. M., Wanders, I., Bertram, R., et al. 1998, *ApJ*, 501, 82
- Planck Collaboration, Ade, P. A. R., Aghanim, N., et al. 2014, *A&A*, 571, A16
- Planck Collaboration, Aghanim, N., Akrami, Y., et al. 2018, arXiv:1807.06209
- Press, W. H., Teukolsky, S. A., Vetterling, W. T., et al. 1992, Cambridge: University Press
- Rafter, S. E., Kaspi, S., Behar, E., Kollatschny, W., & Zetzl, M. 2011, *ApJ*, 741, 66
- Rafter, S. E., Kaspi, S., Chelouche, D., et al. 2013, *ApJ*, 773, 24
- Santos-Lleó, M., Chatzichristou, E., de Oliveira, C. M., et al. 1997, *ApJS*, 112, 271
- Santos-Lleó, M., Clavel, J., Schulz, B., et al. 2001, *A&A*, 369, 57
- Shakura, N. I., & Sunyaev, R. A. 1973, *A&A*, 500, 33
- Shen, Y., & Ho, L. C. 2014, *Nature*, 513, 210
- Shen, Y., Horne, K., Grier, C. J., et al. 2016b, *ApJ*, 818, 30
- Shen, Y., Brandt, W. N., Dawson, K. S., et al. 2015, *ApJS*, 216, 4
- Shen, Y., Richards, G. T., Strauss, M. A., et al. 2011, *ApJS*, 194, 45
- Stern, J., & Laor, A. 2013, *MNRAS*, 431, 836
- Stirpe, G. M., Winge, C., Altieri, B., et al. 1994, *ApJ*, 425, 609
- Sulentic, J. W., Zwitter, T., Marziani, P., & Dultzin-Hacyan, D. 2000, *ApJL*, 536, L5
- Sulentic, J. W., Marziani, P., Zamanov, R., et al. 2002, *ApJ*, 566, L71
- Sun, J., & Shen, Y. 2015, *ApJL*, 804, L15
- Vestergaard, M., & Peterson, B. M. 2006, *ApJ*, 641, 689
- Verner, E., Bruhweiler, F., Verner, D., et al. 2004, *ApJ*, 611, 780
- Wandel, A., Peterson, B. M., & Malkan, M. A. 1999, *ApJ*, 526, 579
- Wang, J.-M., Yan, C.-S., Gao, H.-Q., et al. 2010, *ApJL*, 719, L148
- Wang, J.-M., Du, P., Hu, C., et al. 2014a, *ApJ*, 793, 108
- Wang, J.-M., Du, P., Li, Y.-R., et al. 2014b, *ApJL*, 792, L13
- Wang, J.-M., Qiu, J., Du, P., & Ho, L. C. 2014c, *ApJ*, 797, 65
- Williams, P. R., Pancoast, A., Treu, T., et al. 2018, *ApJ*, 866, 75
- Woo, J.-H., Yoon, Y., Park, S., Park, D., & Kim, S. C. 2015, *ApJ*, 801, 38
- Woo, J.-H., Cho, H., Gallo, E., et al. 2019, *Nature Astronomy*, 3, 755
- Yu, L.-M., Bian, W.-H., Wang, C., et al. 2019, *MNRAS*, 1727
- Zhang, Z.-X., Du, P., Smith, P. S., et al. 2019, *ApJ*, 876, 49

Table 1 (continued)

Objects	$\tau_{H\beta}$	$\log L_{5100}$	FWHM	$\log (M_{\bullet}/M_{\odot})$	$\log \mathcal{M}$	$\log L_{H\beta}$	EW(H β)	$\log L_{[O III]}$	EW([O III])	Ref.
	(days)	(erg s ⁻¹)	(km s ⁻¹)			(erg s ⁻¹)	(Å)	(erg s ⁻¹)	(Å)	
	19.9 ^{+7.3} _{-3.9}	44.52 ± 0.02	1297 ± 12	6.82 ^{+0.14} _{-0.10}	2.75 ^{+0.33} _{-0.32}	42.60 ± 0.03	61.7 ± 5.1	41.75 ± 0.03	8.6 ± 0.7	13
	18.1^{+6.0}_{-4.7}	44.53 ± 0.02	1273 ± 39	6.76^{+0.14}_{-0.15}	2.76^{+0.24}_{-0.24}	42.60 ± 0.03	60.0 ± 5.9	41.78 ± 0.07	9.1 ± 1.4	...
PG 0844+349	32.3 ^{+13.7} _{-13.4}	44.22 ± 0.07	2694 ± 58	7.66 ^{+0.15} _{-0.23}	0.50 ^{+0.57} _{-0.42}	42.56 ± 0.05	111.2 ± 22.1	41.65 ± 0.03	13.9 ± 2.2	5, 6, 10, 15
SDSS J085946	34.8 ^{+19.2} _{-26.3}	44.41 ± 0.03	1718 ± 16	7.30 ^{+0.19} _{-0.61}	1.51 ^{+1.27} _{-0.43}	42.51 ± 0.02	63.1 ± 5.2	41.92 ± 0.04	16.4 ± 2.0	14
Mrk 110	24.3 ^{+5.5} _{-8.3}	43.68 ± 0.04	1543 ± 5	7.05 ^{+0.09} _{-0.18}	0.81 ^{+0.35} _{-0.32}	42.12 ± 0.05	139.6 ± 20.4	41.87 ± 0.05	78.3 ± 5.4	4, 5, 6, 7
	20.4 ^{+10.5} _{-6.3}	43.75 ± 0.04	1658 ± 3	7.04 ^{+0.18} _{-0.16}	0.92 ^{+0.34} _{-0.32}	42.02 ± 0.05	94.8 ± 14.7	41.87 ± 0.05	66.2 ± 4.5	4, 5, 6, 7
	33.3 ^{+14.9} _{-10.0}	43.53 ± 0.05	1600 ± 39	7.22 ^{+0.16} _{-0.16}	0.58 ^{+0.35} _{-0.23}	41.97 ± 0.04	139.4 ± 20.5	41.87 ± 0.05	110.7 ± 8.3	4, 5, 6, 7
	25.6^{+8.9}_{-7.2}	43.66 ± 0.12	1634 ± 83	7.10^{+0.13}_{-0.14}	0.77^{+0.26}_{-0.25}	42.03 ± 0.08	123.8 ± 29.1	41.87 ± 0.05	81.5 ± 21.0	...
SDSS J093302	19.0 ^{+3.8} _{-4.3}	44.31 ± 0.13	1800 ± 25	7.08 ^{+0.08} _{-0.11}	1.79 ^{+0.40} _{-0.40}	42.10 ± 0.05	31.8 ± 10.3	41.26 ± 0.06	4.6 ± 1.5	13
SDSS J093922	11.9 ^{+2.1} _{-6.3}	44.07 ± 0.04	1209 ± 16	6.53 ^{+0.07} _{-0.33}	2.54 ^{+0.71} _{-0.20}	42.09 ± 0.04	53.0 ± 6.7	41.31 ± 0.13	8.8 ± 2.8	9
PG 0953+414	150.1 ^{+21.6} _{-22.6}	45.19 ± 0.01	3071 ± 27	8.44 ^{+0.06} _{-0.07}	0.39 ^{+0.16} _{-0.14}	43.29 ± 0.04	64.7 ± 5.9	42.73 ± 0.02	18.0 ± 1.0	4, 5, 6, 10
SDSS J100402	32.2 ^{+43.5} _{-4.2}	45.52 ± 0.01	2088 ± 1	7.44 ^{+0.37} _{-0.06}	2.89 ^{+0.13} _{-0.75}	43.54 ± 0.01	53.6 ± 1.3	42.45 ± 0.04	4.4 ± 0.4	13
SDSS J101000	27.7 ^{+23.5} _{-7.6}	44.76 ± 0.02	2311 ± 1	7.46 ^{+0.27} _{-0.14}	1.70 ^{+0.31} _{-0.56}	42.77 ± 0.02	52.6 ± 3.4	41.50 ± 0.11	2.8 ± 0.7	13
NGC 3227	3.8 ^{+0.8} _{-0.8}	42.24 ± 0.11	4112 ± 206	7.09 ^{+0.09} _{-0.12}	-1.34 ^{+0.38} _{-0.36}	40.38 ± 0.10	71.0 ± 23.6	40.68 ± 0.10	142.2 ± 22.1	4, 9, 16
SDSS J102339	24.9 ^{+19.8} _{-3.9}	44.09 ± 0.03	1733 ± 29	7.16 ^{+0.25} _{-0.08}	1.29 ^{+0.20} _{-0.56}	42.14 ± 0.03	57.0 ± 5.9	41.32 ± 0.04	8.7 ± 1.0	14
Mrk 142	7.9 ^{+1.2} _{-1.1}	43.56 ± 0.06	1588 ± 58	6.59 ^{+0.07} _{-0.07}	1.90 ^{+0.85} _{-0.86}	41.60 ± 0.04	55.2 ± 9.5	40.86 ± 0.04	10.0 ± 1.3	1, 2, 3
	2.7 ^{+0.7} _{-0.8}	43.61 ± 0.04	1462 ± 2	6.06 ^{+0.10} _{-0.16}	1.96 ^{+0.82} _{-0.82}	41.66 ± 0.05	57.6 ± 8.6	41.24 ± 0.04	21.9 ± 1.4	4, 17
	6.4^{+7.3}_{-3.4}	43.59 ± 0.04	1462 ± 86	6.47^{+0.38}_{-0.38}	1.93^{+0.59}_{-0.59}	41.62 ± 0.06	56.6 ± 6.6	41.06 ± 0.27	18.8 ± 10.5	...
NGC 3516	11.7 ^{+1.0} _{-1.5}	42.79 ± 0.20	5384 ± 269	7.82 ^{+0.05} _{-0.08}	-1.97 ^{+0.41} _{-0.52}	41.06 ± 0.18	94.7 ± 59.2	40.85 ± 0.17	59.5 ± 18.2	4, 9, 16
SBS 1116+583A	2.3 ^{+0.6} _{-0.5}	42.14 ± 0.23	3668 ± 186	6.78 ^{+0.11} _{-0.12}	-0.87 ^{+0.51} _{-0.71}	40.70 ± 0.07	186.8 ± 104.1	40.50 ± 0.06	117.4 ± 61.1	4, 17
Arp 151	4.0 ^{+0.5} _{-0.7}	42.55 ± 0.10	3098 ± 69	6.87 ^{+0.05} _{-0.08}	-0.44 ^{+0.30} _{-0.28}	40.95 ± 0.11	130.0 ± 44.4	40.75 ± 0.07	80.7 ± 14.2	4, 17
NGC 3783	10.2 ^{+3.3} _{-2.3}	42.56 ± 0.18	3770 ± 68	7.45 ^{+0.12} _{-0.11}	-1.58 ^{+0.45} _{-0.59}	41.01 ± 0.18	144.0 ± 83.7	40.95 ± 0.17	126.5 ± 14.6	4, 5, 6, 18
MCG +06-26-012	24.0 ^{+8.4} _{-4.8}	42.67 ± 0.11	1334 ± 80	6.92 ^{+0.14} _{-0.12}	-0.34 ^{+0.37} _{-0.45}	41.03 ± 0.06	114.6 ± 32.5	40.55 ± 0.05	38.7 ± 8.6	1, 2, 3
UGC 06728	1.4 ^{+0.7} _{-0.8}	41.86 ± 0.08	1642 ± 161	5.87 ^{+0.19} _{-0.40}	0.55 ^{+0.92} _{-0.51}	39.85 ± 0.05	49.5 ± 10.8	39.69 ± 0.02	33.8 ± 6.6	19
Mrk 1310	3.7 ^{+0.6} _{-0.6}	42.29 ± 0.14	2409 ± 24	6.62 ^{+0.07} _{-0.08}	-0.31 ^{+0.35} _{-0.39}	40.56 ± 0.10	94.3 ± 38.2	41.05 ± 0.08	293.8 ± 84.8	4, 17
NGC 4051	1.9 ^{+0.5} _{-0.5}	41.96 ± 0.19	851 ± 277	5.42 ^{+0.23} _{-0.53}	0.99 ^{+1.11} _{-1.06}	40.19 ± 0.18	86.8 ± 51.7	40.15 ± 0.17	79.2 ± 14.6	4, 9, 16
	2.9 ^{+0.9} _{-1.3}	41.85 ± 0.18	1145 ± 192	5.87 ^{+0.16} _{-0.37}	0.82 ^{+1.09} _{-1.02}	39.99 ± 0.18	71.7 ± 41.3	40.17 ± 0.17	108.7 ± 7.5	12
	2.1^{+0.9}_{-0.7}	41.90 ± 0.15	1076 ± 277	5.72^{+0.34}_{-0.44}	0.90^{+0.79}_{-0.74}	40.09 ± 0.19	78.6 ± 34.3	40.16 ± 0.12	104.6 ± 24.4	...
NGC 4151	6.6 ^{+1.1} _{-0.8}	42.09 ± 0.21	6371 ± 150	7.72 ^{+0.07} _{-0.06}	-2.81 ^{+0.37} _{-0.57}	40.56 ± 0.20	150.8 ± 100.6	41.60 ± 0.17	1637.3 ± 439.0	4, 5, 6, 20
PG 1211+143	93.8 ^{+25.6} _{-42.1}	44.73 ± 0.08	2012 ± 37	7.87 ^{+0.11} _{-0.26}	0.84 ^{+0.63} _{-0.35}	43.02 ± 0.06	100.2 ± 22.9	42.25 ± 0.03	16.9 ± 3.2	5, 6, 10, 15
Mrk 202	3.0 ^{+1.7} _{-1.1}	42.26 ± 0.14	1471 ± 18	6.11 ^{+0.20} _{-0.20}	0.66 ^{+0.59} _{-0.65}	40.40 ± 0.09	70.6 ± 27.5	40.50 ± 0.07	87.7 ± 25.8	4, 17
NGC 4253	6.2 ^{+1.6} _{-1.2}	42.57 ± 0.12	1609 ± 39	6.49 ^{+0.10} _{-0.10}	0.36 ^{+0.36} _{-0.42}	40.77 ± 0.12	81.1 ± 31.6	41.38 ± 0.12	326.8 ± 37.5	4, 17
PG 1226+023	146.8 ^{+8.3} _{-12.1}	45.92 ± 0.05	3314 ± 59	8.50 ^{+0.03} _{-0.04}	1.37 ^{+0.15} _{-0.14}	44.11 ± 0.03	80.3 ± 10.3	43.24 ± 0.02	10.7 ± 1.3	21
PG 1229+204	37.8 ^{+27.6} _{-15.3}	43.70 ± 0.05	3828 ± 54	8.03 ^{+0.24} _{-0.23}	-1.03 ^{+0.52} _{-0.55}	42.31 ± 0.06	209.7 ± 38.3	41.75 ± 0.03	58.2 ± 6.1	4, 5, 6, 10
NGC 4593	3.7 ^{+0.8} _{-0.8}	42.87 ± 0.18	5143 ± 16	7.28 ^{+0.08} _{-0.10}	-0.73 ^{+0.41} _{-0.52}	41.17 ± 0.18	101.6 ± 59.0	40.64 ± 0.17	30.5 ± 3.2	4, 6, 22
	4.3 ^{+1.3} _{-0.8}	42.38 ± 0.18	4395 ± 362	7.21 ^{+0.13} _{-0.12}	-1.47 ^{+0.41} _{-0.52}	40.73 ± 0.18	115.4 ± 67.6	40.38 ± 0.18	51.8 ± 5.8	9, 23
	4.0^{+0.8}_{-0.7}	42.62 ± 0.37	5142 ± 572	7.26^{+0.09}_{-0.09}	-1.10^{+0.60}_{-0.64}	40.95 ± 0.33	108.3 ± 45.7	40.51 ± 0.22	39.0 ± 14.9	...
IRAS F12397+3333	9.7 ^{+5.5} _{-1.8}	44.23 ± 0.05	1802 ± 560	6.79 ^{+0.27} _{-0.45}	2.26 ^{+0.98} _{-0.62}	42.26 ± 0.04	54.2 ± 8.4	42.35 ± 0.04	66.9 ± 6.8	1, 2, 3
NGC 4748	5.5 ^{+1.6} _{-2.2}	42.56 ± 0.12	1947 ± 66	6.61 ^{+0.11} _{-0.23}	0.10 ^{+0.61} _{-0.44}	40.98 ± 0.10	136.8 ± 50.1	41.33 ± 0.10	300.3 ± 48.4	4, 17
PG 1307+085	105.6 ^{+36.0} _{-46.6}	44.85 ± 0.02	5059 ± 133	8.72 ^{+0.13} _{-0.26}	-0.68 ^{+0.53} _{-0.28}	43.13 ± 0.06	98.4 ± 15.1	42.73 ± 0.02	39.0 ± 2.2	4, 5, 6, 10
MCG +06-30-015	5.3 ^{+1.9} _{-1.8}	41.65 ± 0.23	1958 ± 75	6.60 ^{+0.13} _{-0.18}	-1.28 ^{+0.58} _{-0.73}	39.72 ± 0.13	60.0 ± 36.6	39.96 ± 0.12	104.9 ± 48.6	24
	6.4 ^{+3.1} _{-2.7}	41.64 ± 0.12	1933 ± 81	6.67 ^{+0.17} _{-0.24}	-1.30 ^{+0.46} _{-0.44}	39.97 ± 0.12	108.4 ± 42.8	39.98 ± 0.12	110.5 ± 7.8	25
	5.7^{+1.8}_{-1.7}	41.64 ± 0.11	1947 ± 58	6.63^{+0.12}_{-0.15}	-1.29^{+0.37}_{-0.38}	39.85 ± 0.19	91.0 ± 48.6	39.97 ± 0.09	110.3 ± 8.7	...
NGC 5273	2.2 ^{+1.2} _{-1.6}	41.54 ± 0.16	5688 ± 163	7.14 ^{+0.19} _{-0.56}	-2.50 ^{+1.33} _{-0.67}	39.74 ± 0.11	82.2 ± 37.1	39.49 ± 0.08	46.5 ± 14.5	26
Mrk 279	16.7 ^{+3.9} _{-3.9}	43.71 ± 0.07	5354 ± 32	7.97 ^{+0.09} _{-0.12}	-0.89 ^{+0.30} _{-0.33}	42.12 ± 0.06	132.2 ± 28.7	41.56 ± 0.06	36.9 ± 5.3	4, 5, 6, 27
PG 1411+442	124.3 ^{+61.0} _{-61.7}	44.56 ± 0.02	2801 ± 43	8.28 ^{+0.17} _{-0.30}	-0.23 ^{+0.63} _{-0.38}	42.85 ± 0.03	99.7 ± 8.2	42.18 ± 0.03	21.2 ± 1.2	4, 5, 6, 10
NGC 5548	19.7 ^{+1.5} _{-1.5}	43.39 ± 0.10	4674 ± 63	7.92 ^{+0.03} _{-0.04}	-1.60 ^{+0.46} _{-0.49}	41.79 ± 0.10	128.1 ± 40.3	41.63 ± 0.09	89.1 ± 10.0	4, 5, 6, 28
	18.6 ^{+2.1} _{-2.3}	43.14 ± 0.11	5418 ± 107	8.03 ^{+0.05} _{-0.06}	-1.96 ^{+0.47} _{-0.51}	41.61 ± 0.13	151.3 ± 57.9	41.63 ± 0.09	156.9 ± 24.4	4, 5, 6, 28
	15.9 ^{+2.9} _{-2.5}	43.35 ± 0.09	5236 ± 87	7.93 ^{+0.07} _{-0.08}	-1.65 ^{+0.46} _{-0.49}	41.72 ± 0.10	119.7 ± 37.9	41.63 ± 0.09	97.3 ± 10.4	4, 5, 6, 28
	11.0 ^{+1.9} _{-2.0}	43.07 ± 0.11	5986 ± 95	7.89 ^{+0.07} _{-0.09}	-2.07 ^{+0.47} _{-0.52}	41.52 ± 0.17	144.5 ± 66.7	41.63 ± 0.09	185.1 ± 31.2	4, 5, 6, 28
	13.0 ^{+1.6} _{-1.4}	43.32 ± 0.10	5931 ± 42	7.95 ^{+0.05} _{-0.05}	-1.69 ^{+0.46} _{-0.49}	41.75 ± 0.09	135.9 ± 41.2	41.63 ± 0.09	103.5 ± 11.3	4, 5, 6, 28

Table 1 continued

Table 1 (continued)

Objects	$\tau_{H\beta}$	$\log L_{5100}$	FWHM	$\log(M_{\bullet}/M_{\odot})$	$\log \mathcal{M}$	$\log L_{H\beta}$	EW(H β)	$\log L_{[O III]}$	EW([O III])	Ref.
	(days)	(erg s $^{-1}$)	(km s $^{-1}$)			(erg s $^{-1}$)	(Å)	(erg s $^{-1}$)	(Å)	
	$13.4^{+3.8}_{-4.3}$	43.38 ± 0.09	7378 ± 39	$8.15^{+0.11}_{-0.17}$	$-1.61^{+0.46}_{-0.49}$	41.73 ± 0.10	114.4 ± 37.0	41.63 ± 0.09	91.4 ± 9.8	4, 5, 6, 28
	$21.7^{+2.6}_{-2.6}$	43.52 ± 0.09	6946 ± 79	$8.31^{+0.05}_{-0.06}$	$-1.40^{+0.45}_{-0.48}$	41.82 ± 0.09	102.4 ± 30.2	41.63 ± 0.09	65.9 ± 5.1	4, 5, 6, 28
	$16.4^{+1.2}_{-1.1}$	43.43 ± 0.09	6623 ± 93	$8.15^{+0.03}_{-0.03}$	$-1.53^{+0.45}_{-0.48}$	41.75 ± 0.10	106.3 ± 33.3	41.63 ± 0.09	80.7 ± 7.7	4, 5, 6, 28
	$17.5^{+2.0}_{-1.6}$	43.24 ± 0.10	6298 ± 65	$8.13^{+0.05}_{-0.04}$	$-1.82^{+0.46}_{-0.49}$	41.72 ± 0.10	153.5 ± 50.7	41.63 ± 0.09	125.8 ± 15.3	4, 5, 6, 28
	$26.5^{+4.3}_{-2.2}$	43.59 ± 0.09	6177 ± 36	$8.30^{+0.07}_{-0.04}$	$-1.30^{+0.45}_{-0.48}$	41.87 ± 0.10	98.1 ± 30.0	41.63 ± 0.09	56.5 ± 4.8	4, 5, 6, 28
	$24.8^{+3.2}_{-3.0}$	43.51 ± 0.09	6247 ± 57	$8.28^{+0.05}_{-0.06}$	$-1.42^{+0.45}_{-0.48}$	41.83 ± 0.09	106.6 ± 31.5	41.63 ± 0.09	68.0 ± 6.0	4, 5, 6, 28
	$6.5^{+5.7}_{-3.7}$	43.11 ± 0.11	6240 ± 77	$7.69^{+0.27}_{-0.37}$	$-2.02^{+0.47}_{-0.51}$	41.64 ± 0.13	172.8 ± 66.1	41.63 ± 0.09	170.1 ± 26.8	4, 5, 6, 28
	$14.3^{+5.9}_{-7.3}$	43.11 ± 0.11	6478 ± 108	$8.07^{+0.15}_{-0.31}$	$-2.01^{+0.47}_{-0.51}$	41.55 ± 0.14	139.8 ± 55.7	41.63 ± 0.09	167.5 ± 27.0	4, 5, 6, 28
	$6.3^{+2.6}_{-2.3}$	42.96 ± 0.13	6396 ± 167	$7.70^{+0.15}_{-0.20}$	$-2.24^{+0.49}_{-0.55}$	41.12 ± 0.10	74.4 ± 27.3	41.63 ± 0.09	240.0 ± 53.5	4, 29
	$4.2^{+0.9}_{-1.3}$	43.01 ± 0.11	12771 ± 71	$8.12^{+0.08}_{-0.16}$	$-2.16^{+0.48}_{-0.51}$	41.33 ± 0.10	105.3 ± 35.4	41.63 ± 0.09	211.4 ± 32.6	4, 17
	$12.4^{+2.7}_{-3.9}$	42.99 ± 0.11	11481 ± 574	$8.50^{+0.09}_{-0.17}$	$-2.19^{+0.48}_{-0.53}$	41.27 ± 0.10	96.6 ± 34.4	41.63 ± 0.09	220.3 ± 40.0	4, 16
	$7.2^{+1.3}_{-0.3}$	43.21 ± 0.09	9912 ± 362	$8.14^{+0.08}_{-0.04}$	$-1.87^{+0.45}_{-0.48}$	41.70 ± 0.09	160.1 ± 46.2	41.53 ± 0.09	107.7 ± 7.8	30
	$4.2^{+0.4}_{-0.4}$	43.45 ± 0.09	9496 ± 418	$7.87^{+0.05}_{-0.06}$	$-1.51^{+0.45}_{-0.48}$	41.70 ± 0.09	91.2 ± 26.3	41.55 ± 0.09	64.4 ± 4.5	31
	$13.9^{+11.2}_{-6.2}$	43.30 ± 0.19	7256 ± 2203	$8.08^{+0.16}_{-0.16}$	$-1.76^{+0.31}_{-0.32}$	41.65 ± 0.21	117.8 ± 27.3	41.58 ± 0.07	91.3 ± 36.4	...
PG 1426+015	$95.0^{+29.9}_{-37.1}$	44.63 ± 0.02	7113 ± 160	$8.97^{+0.12}_{-0.22}$	$-1.51^{+0.47}_{-0.28}$	42.83 ± 0.04	80.1 ± 9.2	42.21 ± 0.03	19.2 ± 1.2	4, 5, 6, 10
Mrk 817	$19.0^{+3.9}_{-3.7}$	43.79 ± 0.05	4711 ± 49	$7.92^{+0.08}_{-0.09}$	$-0.81^{+0.35}_{-0.35}$	42.07 ± 0.05	98.0 ± 16.5	41.53 ± 0.05	28.2 ± 1.5	4, 5, 6, 7
	$15.3^{+3.7}_{-3.5}$	43.67 ± 0.05	5237 ± 67	$7.91^{+0.09}_{-0.11}$	$-0.98^{+0.35}_{-0.35}$	42.00 ± 0.06	108.5 ± 20.4	41.53 ± 0.05	37.0 ± 1.9	4, 5, 6, 7
	$33.6^{+6.5}_{-7.6}$	43.67 ± 0.05	4767 ± 72	$8.17^{+0.08}_{-0.11}$	$-0.98^{+0.35}_{-0.35}$	41.92 ± 0.05	91.1 ± 15.3	41.53 ± 0.05	36.9 ± 1.9	4, 5, 6, 7
	$14.0^{+3.4}_{-3.5}$	43.84 ± 0.05	5627 ± 30	$7.94^{+0.09}_{-0.12}$	$-0.73^{+0.35}_{-0.35}$	41.77 ± 0.05	43.2 ± 7.1	41.52 ± 0.05	24.8 ± 1.4	4, 9, 16
	$19.9^{+9.9}_{-6.7}$	43.74 ± 0.09	5348 ± 536	$7.99^{+0.14}_{-0.14}$	$-0.87^{+0.22}_{-0.22}$	41.93 ± 0.14	78.5 ± 34.3	41.53 ± 0.04	31.7 ± 6.4	...
Mrk 1511	$5.7^{+0.9}_{-0.8}$	43.16 ± 0.06	4171 ± 137	$7.29^{+0.07}_{-0.07}$	$-0.34^{+0.24}_{-0.24}$	41.52 ± 0.06	115.5 ± 23.1	41.02 ± 0.05	36.4 ± 4.1	9, 23
Mrk 290	$8.7^{+1.2}_{-1.0}$	43.17 ± 0.06	4543 ± 227	$7.55^{+0.07}_{-0.07}$	$-0.85^{+0.23}_{-0.23}$	41.64 ± 0.06	153.0 ± 29.0	41.64 ± 0.06	150.6 ± 13.2	4, 9, 16
Mrk 486	$23.7^{+7.5}_{-2.7}$	43.69 ± 0.05	1942 ± 67	$7.24^{+0.12}_{-0.06}$	$0.55^{+0.20}_{-0.32}$	42.12 ± 0.04	135.9 ± 20.3	41.33 ± 0.04	22.3 ± 1.8	1, 2, 3
Mrk 493	$11.6^{+1.2}_{-1.2}$	43.11 ± 0.08	778 ± 12	$6.14^{+0.04}_{-0.11}$	$1.88^{+0.33}_{-0.21}$	41.35 ± 0.05	87.4 ± 18.1	40.50 ± 0.05	12.6 ± 1.7	1, 2, 3
PG 1613+658	$40.1^{+15.0}_{-15.2}$	44.77 ± 0.02	9074 ± 103	$8.81^{+0.14}_{-0.21}$	$-0.97^{+0.45}_{-0.31}$	43.00 ± 0.03	86.7 ± 7.6	42.59 ± 0.02	33.7 ± 2.2	4, 5, 6, 10
PG 1617+175	$71.5^{+29.6}_{-33.7}$	44.39 ± 0.02	6641 ± 190	$8.79^{+0.15}_{-0.28}$	$-1.50^{+0.58}_{-0.33}$	42.74 ± 0.05	114.8 ± 15.1	41.84 ± 0.03	14.2 ± 0.8	4, 5, 6, 10
PG 1700+518	$251.8^{+45.9}_{-38.8}$	45.59 ± 0.01	2252 ± 85	$8.40^{+0.08}_{-0.08}$	$1.08^{+0.17}_{-0.17}$	43.78 ± 0.02	78.9 ± 4.5	42.45 ± 0.02	3.7 ± 0.2	4, 5, 6, 10
3C 382	$40.5^{+8.0}_{-3.7}$	43.84 ± 0.10	7652 ± 383	$8.67^{+0.09}_{-0.06}$	$-2.09^{+0.26}_{-0.35}$	42.54 ± 0.03	259.3 ± 64.0	41.92 ± 0.03	61.4 ± 13.9	12
3C 390.3	$23.6^{+6.2}_{-6.7}$	43.68 ± 0.10	12694 ± 13	$8.87^{+0.10}_{-0.15}$	$-3.35^{+0.60}_{-0.65}$	42.29 ± 0.05	206.2 ± 50.7	42.20 ± 0.03	169.1 ± 36.9	4, 5, 6, 30
	$46.4^{+3.6}_{-3.2}$	44.50 ± 0.03	13211 ± 28	$9.20^{+0.03}_{-0.03}$	$-2.12^{+0.51}_{-0.51}$	42.78 ± 0.04	97.1 ± 10.0	42.27 ± 0.03	30.5 ± 0.8	4, 31
	$44.5^{+27.6}_{-17.0}$	44.43 ± 0.58	12796 ± 361	$9.18^{+0.23}_{-0.23}$	$-2.62^{+0.95}_{-0.96}$	42.60 ± 0.35	108.8 ± 58.8	42.24 ± 0.05	31.2 ± 37.8	...
KA 1858+4850	$13.5^{+2.0}_{-2.3}$	43.43 ± 0.05	1820 ± 79	$6.94^{+0.07}_{-0.09}$	$0.75^{+0.25}_{-0.21}$	41.89 ± 0.04	146.9 ± 21.1	41.40 ± 0.03	47.8 ± 5.3	32
NGC 6814	$6.6^{+0.9}_{-0.9}$	42.12 ± 0.28	3323 ± 7	$7.16^{+0.05}_{-0.06}$	$-1.64^{+0.46}_{-0.80}$	40.50 ± 0.28	121.6 ± 112.2	40.26 ± 0.28	69.8 ± 10.0	4, 17
Mrk 509	$79.6^{+6.1}_{-5.4}$	44.19 ± 0.05	3015 ± 2	$8.15^{+0.03}_{-0.03}$	$-0.52^{+0.13}_{-0.14}$	42.61 ± 0.04	132.7 ± 19.1	42.38 ± 0.05	77.7 ± 5.2	4, 5, 6, 7
PG 2130+099	$22.6^{+2.7}_{-3.6}$	44.32 ± 0.04	2101 ± 100	$7.29^{+0.06}_{-0.09}$	$1.40^{+0.24}_{-0.19}$	42.77 ± 0.04	142.4 ± 18.4	42.20 ± 0.04	38.4 ± 4.3	4, 8, 9
NGC 7469	$10.8^{+3.4}_{-1.3}$	43.51 ± 0.11	4369 ± 6	$7.60^{+0.12}_{-0.06}$	$-0.46^{+0.26}_{-0.42}$	41.60 ± 0.10	63.0 ± 21.0	41.69 ± 0.09	77.4 ± 10.8	4, 33

NOTE—The objects are sorted in the order of right ascension. References: (1) Du et al. (2014), (2) Wang et al. (2014a), (3) Hu et al. (2015), (4) Bentz et al. (2013), (5) Collin et al. (2006), (6) Kaspi et al. (2005), (7) Peterson et al. (1998), (8) Grier et al. (2012), (9) Du et al. (2015), (10) Kaspi et al. (2000), (11) Santos-Lleó et al. (1997), (12) Fausnaugh et al. (2017), (13) Du et al. (2018a), (14) Du et al. (2016a), (15) Bentz et al. (2009b), (16) Denney et al. (2010), (17) Bentz et al. (2009a), (18) Stirpe et al. (1994), (19) Bentz et al. (2016a), (20) Bentz et al. (2006), (21) Zhang et al. (2019), (22) Denney et al. (2006), (23) Barth et al. (2013), (24) Bentz et al. (2016b), (25) Hu et al. (2016), (26) Bentz et al. (2014), (27) Santos-Lleó et al. (2001), (28) Peterson et al. (2002), (29) Bentz et al. (2007), (30) Lu et al. (2016), (31) Pei et al. (2017), (32) Dietrich et al. (1998), (33) Dietrich et al. (2012), (34) Pei et al. (2014), (35) Peterson et al. (2014). For the objects with multiple observations, the \mathcal{M} of the individual campaigns are calculated based on the averaged M_{\bullet} .

Table 2. Single-epoch spectral properties

Objects	\mathcal{R}_{Fe}	$\mathcal{D}_{\text{H}\beta}$	$\text{FWHM}_{\text{Fe}}/\text{FWHM}_{\text{H}\beta}$	Asymmetry	EW(He II)	Ref.
					(Å)	
Mrk 335	0.62	1.27 ± 0.05	0.93 ± 0.10	-0.025 ± 0.007	23.9 ± 0.3	1, 2, 3 ^a
PG 0026+129	0.33	1.46 ± 0.09	0.67 ± 0.02	0.036 ± 0.006	13.6 ± 0.2	1, 4, 5 ^a
PG 0052+251	0.12	2.31 ± 0.05	0.51 ± 0.02	-0.037 ± 0.004	28.4 ± 1.2	1, 4, 6 ^a
Fairall9	0.49	2.56 ± 0.03	0.60 ± 0.01	-0.233 ± 0.022	12.1 ± 0.3	1, 8, 9 ^a
Mrk 590	0.45	1.39 ± 0.07	0.58 ± 0.02	-0.025 ± 0.010	47.1 ± 2.7	1, 10 ^a
Mrk 1044	0.99	1.54 ± 0.03	0.74 ± 0.03	0.037 ± 0.003	23.0 ± 0.9	1, 2, 11 ^a
3C 120	0.39	1.86 ± 0.05	0.54 ± 0.12	-0.187 ± 0.020	17.6 ± 1.6	1, 12 ^a
IRAS 04416+1215	1.96	1.44 ± 0.06	0.86 ± 0.04	0.195 ± 0.012	too weak	1, 2, 11 ^a , 13 ^a
Ark 120	0.83	1.65 ± 0.01	0.57 ± 0.11	-0.185 ± 0.020	too weak	1, 12 ^a , 14 ^a
MCG +08-11-011	0.29	1.55 ± 0.11	0.56 ± 0.10	-0.293 ± 0.020	14.6 ± 0.7	15 ^a
Mrk 374	0.88	1.38 ± 0.10	0.32 ± 0.07	-0.100 ± 0.016	5.8 ± 0.4	15 ^a
Mrk 79	0.33	2.10 ± 0.06	0.38 ± 0.18	-0.107 ± 0.018	22.8 ± 0.8	1, 16 ^a
SDSS J074352	1.11	1.60 ± 0.02	0.79 ± 0.02	-0.019 ± 0.003	too weak	11 ^a , 17 ^a
SDSS J075051	1.22	1.54 ± 0.01	1.04 ± 0.06	0.076 ± 0.018	5.7 ± 0.7	11 ^a , 17 ^a
SDSS J075101	0.97	1.52 ± 0.08	1.27 ± 0.10	0.042 ± 0.020	5.7 ± 0.4	1, 11 ^a
Mrk 382	0.75	1.74 ± 0.36	0.91 ± 0.24	0.112 ± 0.019	15.1 ± 0.4	1, 2, 11 ^a , 13
SDSS J075949	1.02	1.49 ± 0.04	0.91 ± 0.03	0.067 ± 0.011	15.4 ± 1.0	11 ^a , 17 ^a
SDSS J080101	1.01	1.61 ± 0.08	0.88 ± 0.02	0.040 ± 0.005	6.9 ± 0.4	1, 11 ^a , 18
SDSS J080131	1.49	1.36 ± 0.03	1.10 ± 0.07	0.059 ± 0.012	5.1 ± 1.3	1, 11 ^a , 19
PG 0804+761	0.61	2.13 ± 0.04	0.53 ± 0.01	-0.007 ± 0.001	1.9 ± 0.1	4, 5 ^a , 6
SDSS J081441	0.46	1.54 ± 0.08	0.71 ± 0.02	-0.008 ± 0.003	20.3 ± 0.8	1, 11 ^a , 17
SDSS J081456	1.31	1.71 ± 0.09	0.77 ± 0.01	0.070 ± 0.007	8.5 ± 0.7	1, 11 ^a , 18
NGC 2617	0.31	2.55 ± 0.18	0.22 ± 0.04	-0.169 ± 0.020	too weak	12, 16 ^a , 20
SDSS J083553	1.57	1.73 ± 0.02	0.87 ± 0.02	0.050 ± 0.006	12.4 ± 0.8	11, 17 ^a
SDSS J084533	1.11	1.38 ± 0.03	0.98 ± 0.03	0.083 ± 0.017	5.5 ± 0.8	1, 11 ^a , 19
PG 0844+349	0.78	1.79 ± 0.04	0.82 ± 0.02	0.071 ± 0.009	9.4 ± 0.8	1, 4, 6, 21 ^a
SDSS J085946	1.39	1.59 ± 0.04	0.92 ± 0.03	0.091 ± 0.020	5.2 ± 1.4	1, 11 ^a , 19
Mrk 110	0.14	1.69 ± 0.09	0.63 ± 0.08	-0.032 ± 0.005	21.0 ± 0.6	1, 21 ^a
SDSS J093302	1.44	1.26 ± 0.02	1.09 ± 0.04	0.052 ± 0.005	16.3 ± 0.6	11 ^a , 17
SDSS J093922	1.48	1.29 ± 0.06	1.17 ± 0.05	-0.051 ± 0.021	16.6 ± 1.0	1, 11 ^a , 18
PG 0953+414	0.27	1.85 ± 0.04	0.50 ± 0.02	-0.009 ± 0.004	7.1 ± 1.8	1, 4, 6, 21 ^a
SDSS J100402	1.17	1.47 ± 0.01	0.81 ± 0.02	0.099 ± 0.007	0.9 ± 0.3	11 ^a , 17
SDSS J101000	2.17	1.64 ± 0.00	0.84 ± 0.03	0.104 ± 0.015	4.8 ± 0.8	11 ^a , 17
NGC 3227	0.46	2.44 ± 0.17	0.71 ± 0.05	-0.011 ± 0.002	33.0 ± 1.5	1, 7, 9 ^a , 22 ^a
SDSS J102339	1.03	1.48 ± 0.04	0.66 ± 0.05	-0.007 ± 0.012	20.5 ± 2.9	1, 11 ^a , 19
Mrk 142	1.14	1.36 ± 0.26	0.95 ± 0.06	0.077 ± 0.005	14.8 ± 0.4	1, 11 ^a
NGC 3516	0.66	2.45 ± 0.17	0.57 ± 0.02	-0.034 ± 0.004	47.7 ± 4.8	1, 7, 9 ^a
SBS 1116+583A	0.59	2.36 ± 0.13	0.66 ± 0.04	-0.029 ± 0.008	31.2 ± 1.1	1, 11 ^a , 23
Arp 151	0.32	1.54 ± 0.04	0.84 ± 0.03	-0.174 ± 0.008	41.3 ± 2.3	1, 23 ^a
NGC 3783	0.04	2.23 ± 0.05	0.51 ± 0.04	-0.088 ± 0.011	57.9 ± 2.5	1, 4, 24, 25 ^a
MCG +06-26-012	1.04	1.70 ± 0.11	0.87 ± 0.07	0.026 ± 0.001	16.7 ± 0.5	1, 2, 13 ^a
UGC 06728	1.11	0.89 ± 0.12	0.60 ± 0.12	-0.069 ± 0.020	14.8 ± 2.9	26 ^a
Mrk 1310	0.46	1.99 ± 0.07	0.68 ± 0.04	-0.005 ± 0.002	32.2 ± 5.2	1, 23 ^a
NGC 4051	1.18	1.97 ± 0.15	1.36 ± 0.12	0.018 ± 0.009	8.9 ± 0.6	1, 7, 27, 28 ^a
NGC 4151	0.22	2.76 ± 0.07	0.34 ± 0.02	0.010 ± 0.017	21.5 ± 1.6	1, 4, 9 ^a , 29
PG 1211+143	0.42	1.35 ± 0.04	0.88 ± 0.03	0.007 ± 0.007	15.2 ± 0.6	1, 4, 6, 21 ^a
Mrk 202	0.57	1.70 ± 0.08	0.73 ± 0.22	-0.015 ± 0.006	21.1 ± 0.7	1, 11 ^a , 23
NGC 4253	0.99	1.48 ± 0.06	0.72 ± 0.03	-0.010 ± 0.001	29.7 ± 1.3	1, 23 ^a
PG 1226+023	0.64	1.97 ± 0.03	0.64 ± 0.02	-0.079 ± 0.004	0.7 ± 0.1	30 ^a
PG 1229+204	0.53	2.38 ± 0.05	0.80 ± 0.02	-0.018 ± 0.007	13.6 ± 1.1	1, 4, 6, 21 ^a
NGC 4593	0.89	2.87 ± 0.66	0.76 ± 0.07	0.043 ± 0.020	6.2 ± 0.2	1, 31 ^a
IRAS F12397+3333	1.48	1.57 ± 0.52	0.97 ± 0.30	0.084 ± 0.010	19.6 ± 0.6	1, 2, 3, 11 ^a

Table 2 continued

Table 2 (continued)

Objects	\mathcal{R}_{Fe}	$\mathcal{D}_{\text{H}\beta}$	$\text{FWHM}_{\text{Fe}}/\text{FWHM}_{\text{H}\beta}$	Asymmetry	EW(He II)	Ref.
					(Å)	
NGC 4748	0.99	1.93 ± 0.08	0.91 ± 0.05	0.011 ± 0.002	34.0 ± 1.3	1, 23 ^a
PG 1307+085	0.21	2.58 ± 0.09	0.40 ± 0.06	-0.207 ± 0.006	15.7 ± 0.7	1, 4, 6 ^a
MCG +06-30-015	0.93	2.01 ± 0.08	1.01 ± 0.49	0.007 ± 0.020	16.6 ± 7.3	23 ^a , 32
NGC 5273	0.58	3.12 ± 0.13	0.71 ± 0.04	0.022 ± 0.005	too weak	1, 22 ^a , 33
Mrk 279	0.55	2.94 ± 0.03	0.52 ± 0.10	0.061 ± 0.006	7.9 ± 0.2	1, 4, 34, 35 ^a
PG 1411+442	0.63	1.58 ± 0.04	0.61 ± 0.04	-0.040 ± 0.004	11.9 ± 0.2	1, 4, 5 ^a , 6
NGC 5548	0.10	2.66 ± 0.33	0.46 ± 0.04	-0.193 ± 0.012	8.4 ± 0.8	1, 4, 11 ^a , 36
PG 1426+015	0.46	2.45 ± 0.09	0.72 ± 0.01	-0.140 ± 0.003	10.4 ± 0.6	1, 4, 6 ^a
Mrk 817	0.69	2.59 ± 0.29	0.87 ± 0.07	-0.163 ± 0.057	22.7 ± 1.1	1, 4, 37, 38 ^a
Mrk 1511	0.80	2.20 ± 0.13	0.75 ± 0.04	-0.003 ± 0.020	6.3 ± 0.2	1, 31 ^a
Mrk 290	0.29	2.57 ± 0.18	0.73 ± 0.03	-0.019 ± 0.004	21.2 ± 1.1	1, 7, 21, 23 ^a
Mrk 486	0.54	1.50 ± 0.06	0.92 ± 0.06	0.035 ± 0.003	15.7 ± 0.2	1, 2, 11 ^a , 13 ^a
Mrk 493	1.13	1.52 ± 0.03	1.00 ± 0.02	0.025 ± 0.018	5.8 ± 0.3	1, 2, 11 ^a , 13 ^a
PG 1613+658	0.38	2.94 ± 0.05	0.35 ± 0.02	-0.167 ± 0.003	7.6 ± 0.4	1, 4, 6 ^a , 21
PG 1617+175	0.74	2.87 ± 0.12	0.98 ± 0.04	-0.068 ± 0.020	1.1 ± 0.2	1, 4, 6 ^a
PG 1700+518	1.32	1.09 ± 0.08	0.69 ± 0.06	0.344 ± 0.024	too weak	1, 4, 5, 6, 27, 39
3C 382	0.31	1.87 ± 0.13	0.71 ± 0.13	-0.182 ± 0.011	too weak	15, 35 ^a
3C 390.3	0.12	2.62 ± 0.66	0.47 ± 0.08	-0.062 ± 0.020	too weak	1, 18, 40, 41
KA 1858+4850	0.11	2.13 ± 0.13	0.46 ± 0.05	0.015 ± 0.020	35.2 ± 9.2	1, 42 ^a
NGC 6814	0.45	1.73 ± 0.03	0.73 ± 0.01	-0.010 ± 0.020	23.8 ± 0.3	1, 18, 23 ^a
Mrk 509	0.13	1.94 ± 0.01	0.59 ± 0.24	-0.057 ± 0.022	44.0 ± 10.0	1, 4, 9 ^a , 37
PG 2130+099	0.96	1.39 ± 0.11	0.95 ± 0.06	0.017 ± 0.001	14.2 ± 0.2	1, 5 ^a , 43
NGC 7469	0.43	1.49 ± 0.18	0.83 ± 0.24	-0.316 ± 0.032	17.5 ± 0.7	1, 27, 44, 45 ^a

NOTE—References: (1) Du et al. (2016b), (2) Hu et al. (2015), (3) Du et al. (2014), (4) Collin et al. (2006), (5) Hu et al. (2019), (6) Kaspi et al. (2000), (7) Denney et al. (2010), (8) Santos-Lleó et al. (1997), (9) the spectrum from the archive of Hubble Space Telescope, (10) Marziani et al. (2003), (11) the spectrum from the SDSS archive, (12) Du et al. (2018b), (13) Wang et al. (2014a), (14) Doroshenko et al. (2008), (15) Fausnaugh et al. (2017), (16) Brotherton et al. (2019), (17) Du et al. (2018a), (18) Du et al. (2015), (19) Du et al. (2016a), (20) Fausnaugh et al. (2017), (21) Boroson & Green (1992), (22) Ho et al. (1995), (23) Bentz et al. (2009a), (24) Stirpe et al. (1994), (25) Jones et al. (2009), (26) Bentz et al. (2016a), (27) Kollatschny & Zetzl (2011), (28) Moustakas, & Kennicutt (2006), (29) Bentz et al. (2006), (30) Zhang et al. (2019), (31) Barth et al. (2013), (32) Hu et al. (2016), (33) Bentz et al. (2014), (34) Santos-Lleó et al. (2001), (35) Marziani et al. (2003), (36) Peterson et al. (2002), (37) Peterson et al. (1998), (38) Ilić et al. (2006), (39) Bian et al. (2010), (40) Dietrich et al. (2012), (41) Du et al. (2018b), (42) Pei et al. (2014), (43) Grier et al. (2012), (44) Peterson et al. (2014), (45) Kim et al. (1995). ^a The spectral properties are measured from the spectrum in the reference if not found in the literatures. As in Du et al. (2016b), we adopt 20% of the \mathcal{R}_{Fe} as its error bar.